ADVANCED OPTICAL MATERIALS
www.advopticalmat.de

Leveraging of MEMS Technologies for Optical Metamaterials Applications

*Zhihao Ren, Yuhua Chang, Yiming Ma, Kailing Shih, Bowei Dong, and Chengkuo Lee**

Tunable metamaterial devices have experienced explosive growth in the past decades, driving the traditional electromagnetic (EM) devices to evolve into diversified functionalities by manipulating EM properties such as amplitude, frequency, phase, polarization, and propagation direction. However, one of the bottlenecks of these rapidly developed metamaterials technologies is limited tunability caused by the intrinsic frequency-dependent property of exotic tunable material. To overcome such limitation, the microelectromechanical system (MEMS) enabling micro/nanoscale manipulation is developed to actively control "meta-atom" in terahertz and infrared region, which brings frequency-scalable tunability and complementary metal-oxide-semiconductor-compatible functional meta-devices. Beyond tunability, novel chemical sensing platforms of molecular identification and dynamic monitoring of the biochemical process can be achieved by integrating micro/nanofluidics channels with metamaterial resonators. Additionally, incorporating metamaterial absorbers with MEMS resonators brings another research interest in MEMS zero-power devices and radiation sensors. Furthermore, moving from 2D metasurfaces to 3D metamaterials, enhanced EM properties like novel resonance mode, giant chirality, and 3D manipulation reinforce the application in biochemical and physical sensors as well as functional meta-devices, paving the way to realize multi-functional sensing and signal processing on a hybrid smart-sensor microsystem for booming healthcare, environmental monitoring, and the Internet of Things applications.

1. Introduction

In recent years, metamaterials with artificially engineered sub-wavelength structure have shown great advancement in numerous interesting electromagnetic (EM) properties such as artificial magnetism,[1,2] negative refractive index,[3–7] metalenses,[8–13] wavelength selective absorption,[14–21] slow light behavior,[22–28] and chirality.[29–32] To actively control the metamaterial, various efforts have been developed such as the optically pumped photoconductive materials,[33,34] electrically controlled refractive index of liquid crystals,[35,36] biasing of doped semiconductor devices[37–40] or graphene,[41–43] thermally controlled refractive index of materials,[44,45] conductivity control in phase change materials,[46,47] magnetically controlled active materials,[48,49] and so on.[50–53] However, the intrinsic frequency-dependent property of these materials hinders the spectral scalability. Some exotic materials are not complementary metal-oxide-semiconductor (CMOS) compatible and require bulky equipment for external stimulus, which limits commercialization and miniaturization. On the other hand, the most ideal and straightforward method for the reconfiguration is to geometrically modify the parameters of the unit cell, which is also called the meta-atom that determines the property of metamaterials. Furthermore, in terms of feature size, the microelectromechanical system (MEMS) and micro/nanofluidics enable micro/nanoscale mechanical manipulation and are suitable for meta-atom in terahertz (THz) and IR region, which brings the diversified applications in metamaterial functional device. The advancement in MEMS and micro/nanofluidics offers a wide palette of actuators and liquid channels to enable both in-plane and out-of-plane reconfigurations with varying performance characteristics that could be realized based on the application requirements, ranging from fundamental functions, such as the modulation of intensity, frequency, bandwidth, and electromagnetically induced transparency (EIT) phenomenon, to more sophisticated devices, such as tunable waveplate, logic operation, and resonant cloaking. Beyond tunability, novel chemical sensing platforms in terms of gas, liquid, and thin film sensing of biomolecules can be realized through metamaterials resonators or the hybrid sensing platforms

Z. Ren, Y. Chang, Y. Ma, K. Shih, B. Dong, Prof. C. Lee
Department of Electrical and Computer Engineering
National University of Singapore
4 Engineering Drive 3, Singapore 117576, Singapore
E-mail: elelc@nus.edu.sg
Z. Ren, Y. Chang, Y. Ma, K. Shih, B. Dong, Prof. C. Lee
Center for Intelligent Sensors and MEMS
National University of Singapore
E6#05-11F, 5 Engineering Drive 1, Singapore 117608, Singapore
B. Dong, Prof. C. Lee
NUS Graduate School for Integrative Science and Engineering
National University of Singapore
28 Medical Drive, Singapore 117456, Singapore
Z. Ren, Y. Chang, Y. Ma, K. Shih, B. Dong, Prof. C. Lee
NUS Suzhou Research Institute
Suzhou Industrial Park, Suzhou 215123, China
The ORCID identification number(s) for the author(s) of this article can be found under https://doi.org/10.1002/adom.201900653.

DOI: 10.1002/adom.201900653

integrated with gas enrichment layers or micro/nanofluidics. Multiple sensor pixel arrays with ultra-broadband operation frequencies enable the molecular identification and dynamic monitoring of the biochemical process through detecting multiple characteristic absorption fingerprints at multiple frequencies of different types of molecules. The advanced signal processing algorithm for a large amount of data from sensor array readout provides an opportunity for the aid of artificial intelligence (AI) to accumulate the intelligence of smart sensor platforms in healthcare, environmental monitoring, and the Internet of Things (IoT) applications. Additionally, incorporating metamaterial absorbers with MEMS resonators brings another research interest in MEMS zero-power devices and radiation sensors. Such a hybrid physical sensing platform shows advantages in compact feature size, wavelength-selective detection, and polarization sensitive operation thanks to the diversified EM properties of plasmonic metamaterial absorber design. Furthermore, moving from 2D metasurfaces to 3D metamaterials, enhanced EM properties like novel resonance mode, giant chirality, and 3D manipulation reinforce the application in biochemical and physical sensors as well as functional meta-devices. In this article, a roadmap of the development of MEMS metamaterials in functional devices,[54–63] chemical sensors,[64–69] and physical sensors[70–75] is summarized. (**Figure 1**).

In 2009, out-of-plane thermal actuator consisting of bimorph cantilevers was first reported by Prof. R. D. Averitt and his group members to control split-ring-resonator (SRR) unit cells to achieve simultaneous control of both electrical and magnetic responses at THz frequencies.[54] In the same year, surface enhanced IR spectroscopy sensing of monolayer octadecanethiol (ODT) was reported using plasmonic SRR metamaterial, which enabled ultrasensitive label-free detection of molecules.[64] Besides, wavelength-selective metamaterial absorber was developed to enhance the performance of microbolometer at mid-IR.[70] Moving to 2011, in-plane electrostatic comb drive actuator was demonstrated to manipulate two SRRs: one on a movable electrode and the other on a fixed electrode.[55] In physical radiation sensing, Tao et al. integrated frequency selective metamaterial absorber with MEMS cantilever to enhance the performance of THz MEMS thermal detector.[71] Later in 2012, a stretchable substrate was reported to achieve mechanically in-plane tunable metamaterial.[56] In biochemical sensing, enhanced sensitivity has been shown on a Fano-resonant metamaterial by breaking the symmetry of the geometric structure.[65] Moving forward, microfluidic integrated nanoantenna in surface-enhanced IR absorption (SEIRA) spectroscopy was optimized using temporal coupled-mode theory (TCMT) to achieve dynamic monitoring of protein biomolecular process in 2013 by Prof. H. Altug and her group members.[66] In 2014, Prof. C. Lee and his group members demonstrated out-of-plane tunable metamaterial using electrostatic force and pressure difference induced by the fluidic flow.[57,58] Then in 2015, liquid metal tunable metamaterial was developed by Prof. A. Liu and Prof. N. Zheludev's research group.[60] Moving from fluidic tuning to gas flow tuning, a pneumatically tunable chiral metamaterial was reported in this year.[59] Additionally, the plasmonic enhanced IR focal plane array (FPA) detector was developed.[72] In 2016, out-of-plane electromagnetically tunable cut-wire and SRR metamaterial were demonstrated as a THz switch. Lipid membrane biomolecular process was monitored by plasmonic nanoantenna SEIRA with a microfluidic channel.[67] Metamaterial absorber on an aluminum nitride (AlN) piezoelectric resonator was used to achieve infrared MEMS detector.[73] Later in 2017, an optomechanical THz detector with SRR metamaterial absorber was reported.[74] In addition to radiation detection, metamaterial was also utilized

Zhihao Ren received his B.Sc. degree from the School of Physics at the University of Electronic Science and Technology of China (UESTC), Chengdu, China, in 2017. After that he received his M.Sc. degree in electrical and computer engineering (ECE) from National University of Singapore (NUS). He is currently a Research Engineer in the Department of ECE, NUS. His research interests are focused on mid-IR chemical sensors on metamaterials and nanophotonics for biomedical application.

Bowei Dong received his B.S. degree in physics and mathematics from the School of Physics and Mathematical Sciences of Nanyang Technological University, China. He is currently a Ph.D. student in NUS Graduate School for Integrative Sciences and Engineering. His research interest includes mid-IR photonics for healthcare and environmental monitoring applications.

Chengkuo Lee received his Ph.D. degree in precision engineering from The University of Tokyo, Japan, in 1996. Currently, he is the Director of Center for Intelligent Sensors and MEMS, and an Associate Professor in the Department of Electrical and Computer Engineering, National University of Singapore, Singapore. In 2001, he co-founded Asia Pacific Microsystems, Inc., where he was the Vice President. From 2006–2009, he was a senior member of the technical staff at the Institute of Microelectronics, A-STAR, Singapore.

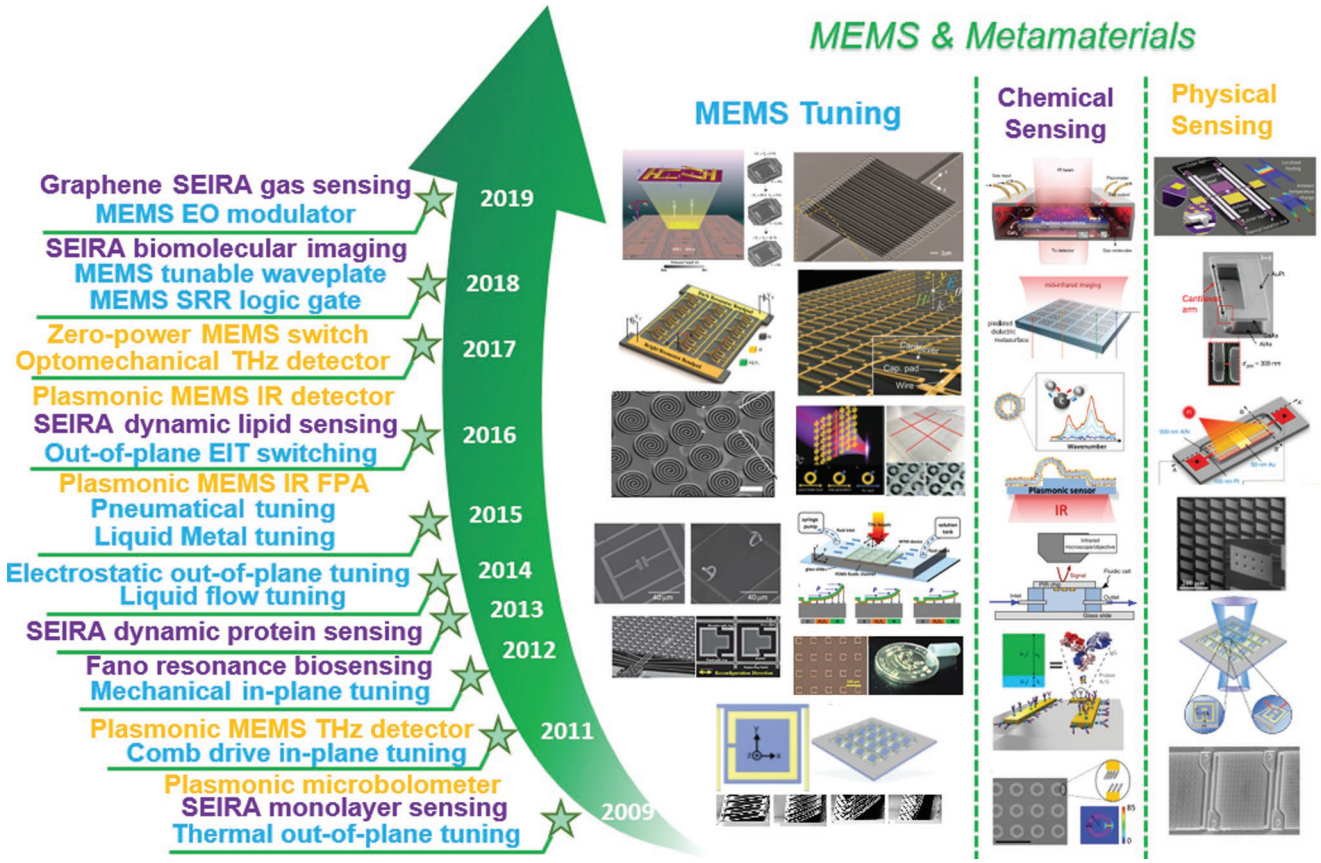

Figure 1. A roadmap of the development of MEMS and metamaterials in the past 10 years. Reproduced with permission.[54] Copyright 2009, American Physical Society. Reproduced with permission.[55] Copyright 2011, Wiley-VCH. Reproduced with permission.[56] Copyright 2012, Wiley-VCH. Reproduced with permission.[57] Copyright 2014, Springer Nature. Reproduced with permission.[58] Copyright 2014, AIP Publishing. Reproduced with permission.[59] Copyright 2015, Springer Nature. Reproduced with permission.[60] Copyright 2015, Wiley-VCH. Reproduced with permission.[61] Copyright 2016, Wiley-VCH. Reproduced with permission.[62] Copyright 2018, Optical Society of America. Reproduced with permission.[63] Copyright 2018, Springer Nature. Reproduced with permission.[64] Copyright 2009, AIP Publishing. Reproduced with permission.[65] Copyright 2012, Springer Nature. Reproduced with permission.[66] Copyright 2013, Springer Nature. Reproduced with permission.[67] Copyright 2016, American Chemical Society. Reproduced with permission.[68] Copyright 2018, The American Association for the Advancement of Science. Reproduced with permission.[69] Copyright 2019, Springer Nature. Reproduced with permission.[70] Copyright 2009, Optical Society of America. Reproduced with permission.[71] Copyright 2011, Optical Society of America. Reproduced with permission.[72] Copyright 2016, AIP Publishing. Reproduced with permission.[73] Copyright 2016, Springer Nature. Reproduced with permission.[74] Copyright 2017, Springer Nature. Reproduced with permission.[75] Copyright 2017, Springer Nature.

in a zero-power MEMS switch.[75] By further combining MEMS tunability and metamaterial's unique EM property, logic gate and tunable waveplate were demonstrated in 2018.[63] For SEIRA chemical sensing, biomolecular barcoding using metamaterial sensor array was proposed to achieve efficient molecules identification in the mid-IR fingerprint region.[68] Moving forward, in 2019, MEMS-based electrooptical modulator was achieved using bilayer nanowire consisting of Si and indium tin oxide (ITO).[76] Graphene metamaterial was demonstrated as a multifunctional platform in gas sensing, which can absorb gas molecules as well as provide plasmonic resonance.[69]

This review is organized into four major parts. In Section 2, the tuning mechanism of the MEMS metamaterials will be discussed, and the innovative application of MEMS tunable metamaterial functional devices will be introduced. Then, the metamaterial in chemical sensing application will be reviewed in Section 3 in terms of different working frequencies from IR, Gigahertz (GHz) to THz. Besides, a comprehensive discussion on metamaterial enhanced MEMS zero-power devices and physical sensors will be conducted in Section 4. Furthermore, 3D metamaterials with enhanced EM properties will be summarized in Section 5, followed by concluding remarks on outlooks.

2. MEMS Tunable Metamaterials

2.1. MEMS Tuning Mechanisms in Metamaterials

The MEMS reconfigurable metamaterials are classified by their actuator mechanisms. The in-plane movement of the unit cell is mainly achieved by comb-drives, which are interdigitated lateral combs offering bidirectional displacement. Liu and his co-workers have developed several types of comb-drive actuated metamaterials.[77–79] As shown in **Figure 2**a, semi-square SRR can be reshaped into three states with half of the split ring fixed

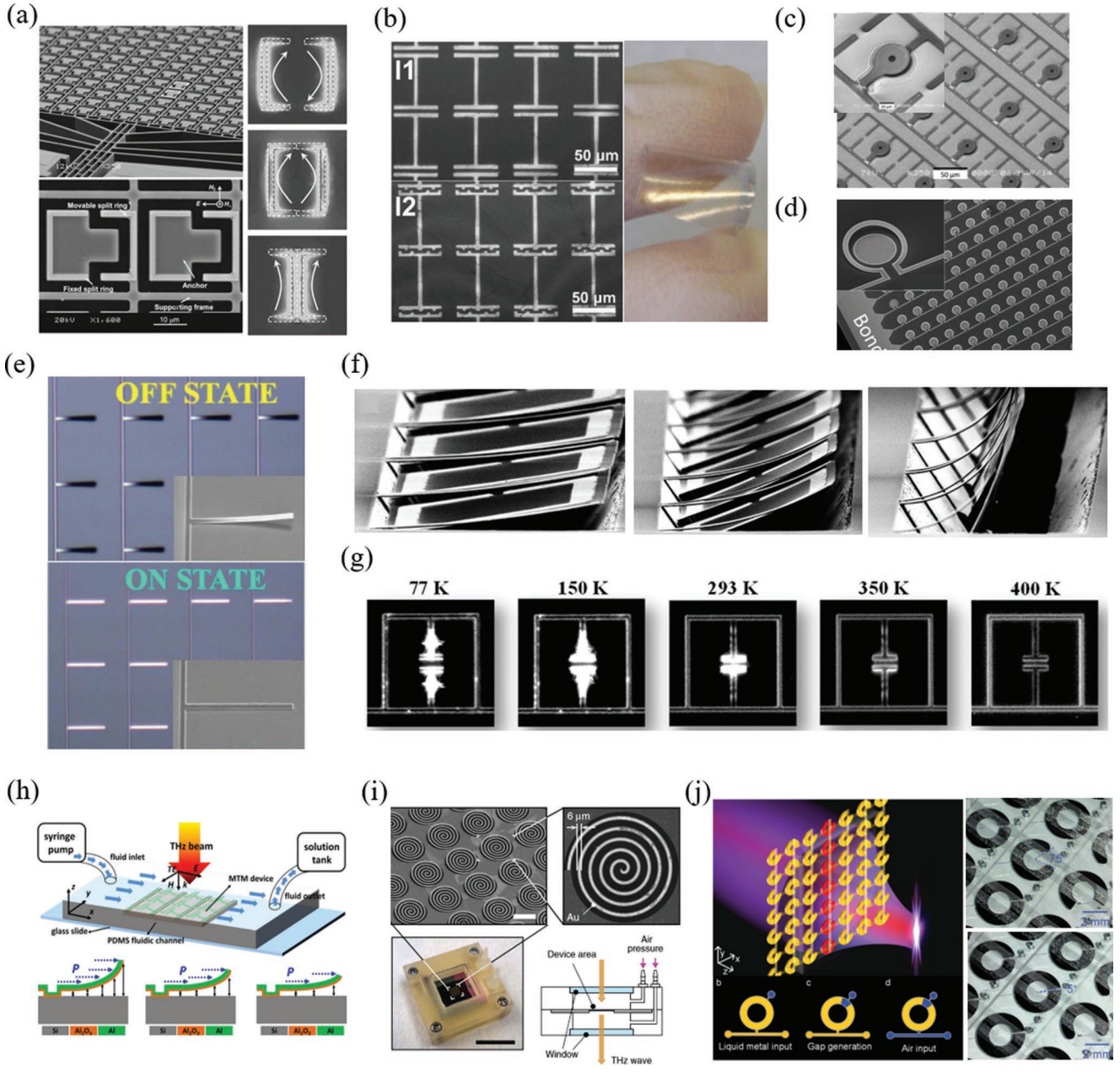

Figure 2. An overview of the MEMS actuating mechanisms in metamaterials. a) In-plane comb-drive actuated semi-square split ring. b) Mechanically tunable I-shape metamaterial sandwiched between flexible PDMS substrates. Pre-stressed SRR actuated by c) electrostatic force and d) electrothermal actuator. e) Pre-stressed cantilever metamaterial driven by electrostatic force. Thermally reconfigurable pre-stressed f) SRR and g) microcantilever-based metamaterial. h) Flow tunable mirror-like T-shape metamaterial. i) Pneumatic actuated chiral metamaterial. j) Randomly addressable SRR tuned pneumatically by liquid metal in microfluidic channel. (a) Reproduced with permission.[55] Copyright 2011, Wiley-VCH. (b) Reproduced with permission.[84] Copyright 2011, AIP Publishing. (c) Reproduced with permission.[86] Copyright 2015, IEEE. (d) Reproduced with permission.[87] Copyright 2014, AIP Publishing. (e) Reproduced with permission.[88] Copyright 2015, IEEE. (f) Reproduced with permission.[54] Copyright 2009, American Physical Society. (g) Reproduced with permission.[90] Copyright 2017, AIP Publishing. (h) Reproduced with permission.[91] Copyright 2014, AIP Publishing. (i) Reproduced with permission.[59] Copyright 2015, Springer Nature. (j) Reproduced with permission.[60] Copyright 2015, Wiley-VCH.

and the other half moveable. The tuning of the air gap between two rings induces the different directions of surface current and thus the intensity of magnetic resonance, switching the effective permeability from negative to positive.[55] A broadside-coupled two-layer SRR, where the air gap between fixed bottom layer and comb-drive actuated top layer is formed by flip-chip bonder, is proposed by Zhao et al.[80] The 18 μm lateral displacement between two vertically separated layers results in 100 GHz frequency shift. The other in-plane actuator scheme is the thermal actuator.[81,82] There are mainly two types: the U-shape actuator that deploys hot-cold arms of different widths and the V-shape chevron beam that buckles along the tip when

current flows through.[82] Lalas et al. designed a U-shape electrothermal actuator with two hot arms to drive the gap inside SRR. The V-shape actuator designed by Li et al. can drive the slabs beside the two-cut SRR to continuously sweep resonance frequency from 1.374 to 1.574 THz.[81]

Another possibility of mechanical tunability is the stretching of an elastic substrate.[83–85] As illustrated in Figure 2b, Li et al. experimentally demonstrated interdigitated I-shape metamaterial, where Au is deposited directly onto a polydimethylsiloxane (PDMS) substrate and encapsulated by a top PDMS thin film.[84] The mechanical stretching along the polarization expands the gap width and consequently reduces the gap capacitance. A repeatable 8.3% tuning in dipole resonance frequency was realized with 10% strain and 650 μm stretching. The metamaterial absorber, consisting of two dielectric resonators on a conductive rubber layer, shows a reversible frequency tuning of 410 MHz when the 180% strain along magnetic field increases the separation and reduces the coupling between the magnetic dipoles.[85]

Besides the in-plane reconfiguration, part of the unit cell can also move in the direction perpendicular to the substrate. Such an out-of-plane movement is realized by the residue stress in bimaterial rings or cantilevers. The stress in the bilayers can be caused due to various reasons, such as lattice mismatch between the layers, thermal budget in the fabrication process, and recipe used for thin film deposition. However, the major contributor is the temperature variations in the fabrication process. The strong mismatch between the thermal expansion coefficients (TECs) of the two materials causes the residual stress to build up in the structure. When the sacrificial layer is released, this stress is manifested as the out-of-plane deformation toward the material with smaller TEC. This initial noncontact state is the off-state as the air gap reduces the effective capacitance and blue-shifts the frequency. When a voltage is applied between the lightly doped substrate and the deformed part of the unit cell, the electrostatic force brings the deformed part into physical contact with the substrate, which is the on-state and also called the "pull in" or "snap down" state. In Figure 2c, Han et al. utilized the residue stress in Au and SiO_2 bilayers to tilt up the SRR, which functions as a tunable THz filter of high contrast ratio and a modulator of 2 kHz.[86] A similar pre-stressed omega ring was developed by Ho et al. in Figure 2d[87] but actuated electrothermally. Another essential building block in the out-of-plane tuning scheme is the cantilever, as shown in Figure 2e,[88] which consists of top layer Al and bottom layer Al_2O_3. Due to its simplicity, the tip-end displacement can be analytically expressed as[89]

$$\frac{1}{r}=\frac{6n(1+n)(m\sigma_{\mathrm{Al}}-\sigma_{\mathrm{d}})}{t_{\mathrm{Al}}E_{\mathrm{Al}}\left[K+3mn\left(1+n^{2}\right)\right]} \tag{1}$$

where $K=1+4mn+6mn^2+4mn^3+m^2n^4$; $m=E_{\mathrm{Al}}/E_{\mathrm{d}}$; $n=t_{\mathrm{Al}}/t_{\mathrm{d}}$. The tip displacement can be calculated as: $\delta=r\left[1-\cos\left(l_{\mathrm{c}}/r\right)\right]$, where E_{Al} and E_{d} are the Young's modulus and σ_{Al} and σ_{d} are the residual stresses of Al and Al_2O_3 material layers, respectively; l_{c} is the length of the cantilever. The influences of the various geometrical parameters of the cantilever are also investigated experimentally and systematically.

Since such pre-stressed bilayers are intrinsically a bimorph thermal actuator, the displacement can also be tuned by the temperature. Tao et al. demonstrated the modulation in transmission intensity of both magnetic and electric resonances by thermally actuating the orientation of SRR, as shown in Figure 2f.[54] In Figure 2g, Pitchappa et al. demonstrated bidirectional thermally reconfigurable microcantilever metamaterial where the resonance frequency shifts continuously from 0.42 THz at 77 K to 0.32 THz at 400 K, showing a 37.5% broader tunable range than previously reported works.[90] When the temperature increases further above the room temperature, cantilevers bend downward to the substrate, leading to better field confinement, reduced radiation loss, and enhanced quality (Q) factor.

In addition to the electrostatic force that can attract the released microcantilever down to the substrate, liquid force is also incorporated to bend it. In the microcantilever-based T-shape metamaterial developed by Lin et al. in Figure 2h, a PDMS microfluidic channel is integrated and linked with a syringe pump for flow control.[91] The liquid force is applied to the cantilever and is proportional to the volumetric flow rate. Assuming the liquid under the cantilevers is quiescent, the cantilever tips deflect downward as a result of the constant pressure beneath the cantilevers and linearly increased pressure above the cantilevers. A resonance frequency shift of 0.30 THz was realized with the flow rate changing from 0 to 5 mL min^{-1}.

Kan et al. demonstrated a pneumatic-actuated handedness-switchable chiral metamaterial in Figure 2i for polarization modulation, where the pressure difference deforms the released microstructures.[59] The pneumatic actuation mechanism has the advantage of achieving bidirectional actuation by reversing the pressure difference. Furthermore, metal lines are not required to provide the external stimulus; consequently, interference caused by the routing metal lines is avoided. By changing the pressure difference across the top and bottom surfaces, the in-plane released spiral structures deform upward and downward with continuously varying height to form an optical activity that rotates the polarization state. A strong optical resonance at 1.0 THz provides a maximum ellipticity angle of 28°.

A random access reconfigurable metamaterial (RARM) was demonstrated as a flat lens by Zhu et al., using an array of cavities filled with liquid metal and controlled by pneumatic valves, as shown in Figure 2j.[60] Each unit cell consists of liquid metal rings and two metal gratings that enhance the cross-polarization transmission. 2π phase range can be achieved by tuning the gap openings and the symmetric axes of rings, while over 70% transmission can be maintained. The diffraction efficiency was measured to be ≈10% while the focal length was adjustable from 5.1 λ with full width at half maximum (FWHM) from 2.1 to 15.2 λ.

2.2. MEMS Metamaterials Functional Devices

The combination of advanced MEMS technology with metamaterials enables various applications, ranging from fundamental functions, such as the modulation of intensity,[76,92–95] frequency,[87,96–100] bandwidth,[101] and EIT phenomenon,[61,102,103] to more sophisticated devices, such as tunable waveplate,[62,104] logic operation,[63,105] and resonant cloaking.[106]

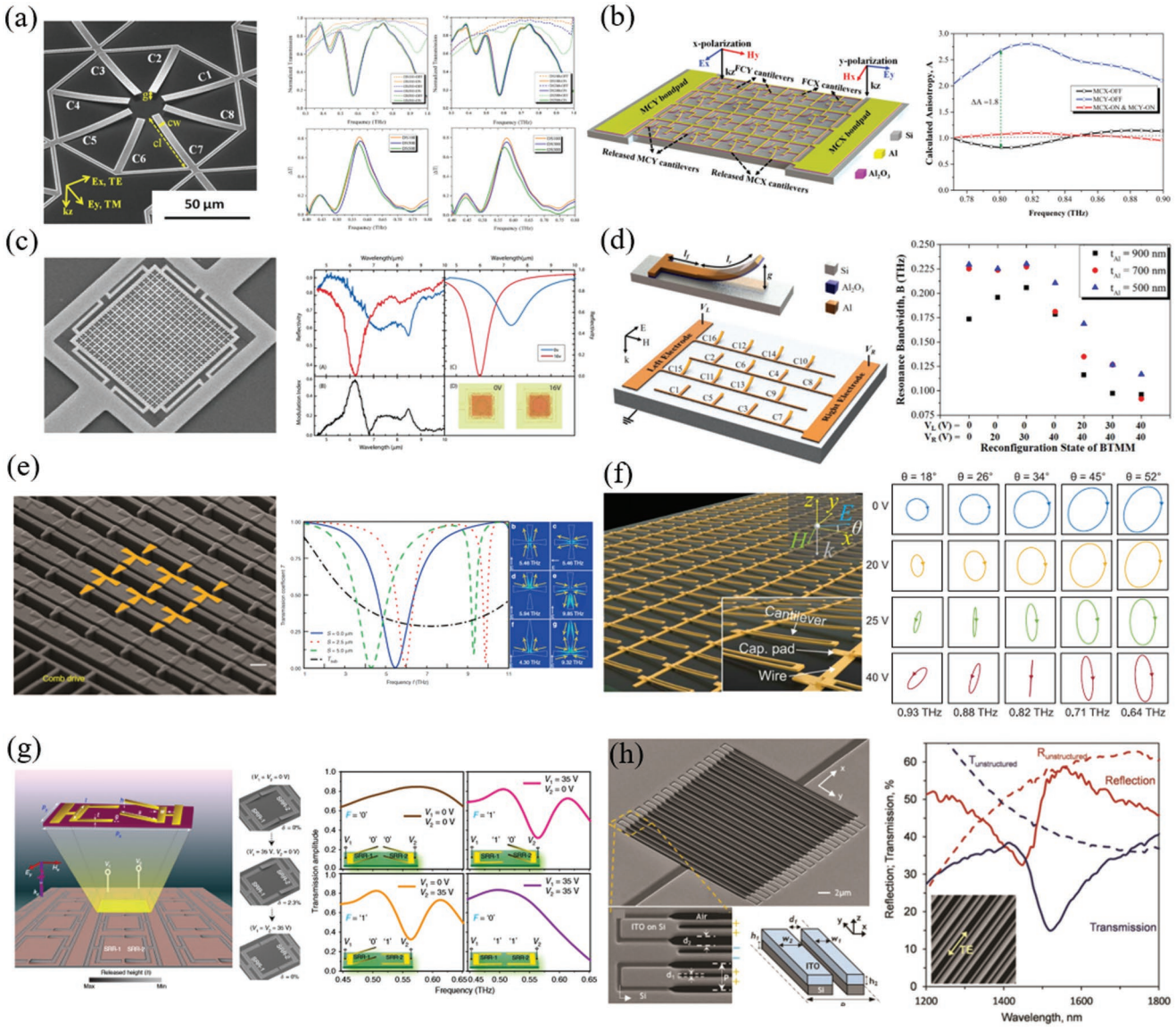

Figure 3. Applications for the MEMS actuated metamaterial. a) Octagon ring metamaterial for uniaxially isotropic switch, b) microcantilever based digital metamaterial for anisotropic swtich, c) Baninet metamaterial for electrostatic intensity modulation, d) microcantilever resonators for bandwidth control, e) comb-drive actuated Maltese-cross metamaterial for tunable terahertz anisotropy, f) cantilever array based metamaterial as tunable waveplate, g) multiple input–output SRR for XOR and XNOR logic operations, h) Si/ITO nanowire mematerial for intensity modulation in near-infrared.[76] (a) Reproduced with permission.[107] Copyright 2015, Springer Nature. (b) Reproduced with permission.[108] Copyright 2016, Wiley-VCH. (c) Reproduced with permission.[94] Copyright 2013, Wiley-VCH. (d) Reproduced with permission.[101] Copyright 2017, AIP Publishing. (e) Reproduced with permission.[78] Copyright 2012, Springer Nature. (f) Reproduced with permission.[62] Copyright 2018, Optical Society of America. (g) Reproduced with permission.[63] Copyright 2018, Springer Nature. (h) Reproduced with permission.[76] Copyright 2019, Wiley-VCH.

An Isotropic switch was demonstrated by Pitchappa et al. using the octagon ring based on pre-stressed microcantilever, as presented in **Figure 3**a.[107] Two conditions should be satisfied for the polarization independence: rotational symmetry of the unit cell and actuation direction that is parallel to the propagation direction of the incident wave. Such polarization independence is preserved in all reconfiguration states by the octagon ring for both electrical inductive-capacitive (ELC) resonance and dipolar resonance. A frequency tuning range of 0.16–0.37 THz and a transmission intensity modulation of more than 0.2 and 0.7 are shown for the ELC and dipolar resonances, respectively, for both transverse electric (TE) and transverse magnetic (TM) modes.

An anisotropic digital metamaterial was proposed by Pitchappa et al. in Figure 3b to switch either only *x*-polarized incidence or only *y*-polarized incidence or both *x*- and *y*-polarized incidence or neither *x*- nor *y*-polarization of incidence THz waves, gaining full control over anisotropy.[108] Its unit cell consists of four geometrically identical T-shaped pre-stressed microcantilevers placed with $\pi/2$ rotational symmetry, among which two are movable and the other two are fixed to the

substrate. The anisotropy defined as the intensity ratio between x and y polarization was measured as 2.65 at 0.8 THz.

In Figure 3c by Liu and Padilla, a babinet metamaterial and the dielectric layer beneath it are suspended over the opaque ground plane, which grants zero transmission.[94] Upon the application of a snap-down voltage at 16 V, the electrostatic force will pull the metallic-dielectric layer into contact with the ground plane, switching on minimum reflectivity and maximum absorptivity. At this state, the impedance matches between the incident radiation and the metamaterial. The restoring force from the actuator brings the layer back to the off state when the voltage is off. A modulation index of 56% at 6.2 μm was achieved with modulation speeds up to 30 kHz.

The resonance bandwidth is also tunable as demonstrated by Shih et al. in a pre-stressed microcantilever array shown in Figure 3d, in addition to the abovementioned switch-like functions.[101] The unit cell is a 4 × 4 cantilever array of equal total length and width. However, the release lengths, and as a result, the out-of-plane tip displacements, are gradually varied, which enable a broadband response of around 175 GHz in the initial off state. When a voltage is applied, the out-of-plane gap is closed, and all the 16 cantilevers resonate at the same resonance frequency, leading to a narrow band response of 90 GHz.

Besides the basic functions mentioned in Figure 3a–d, more advanced features have been realized. Zhu et al. utilized the comb-drive actuated Maltese-cross as shown in Figure 3e, where one of the trapezoid metal beams is moveable to break the fourfold symmetry and introduce anisotropy.[78] The overall Fano mode is the result of the coupling between the dipole resonance of the Maltese cross and the Fabry–Perot resonance from the substrate. The tunable anisotropy comes from the dipole resonance mode because the surface current is concentrated on two beams that are parallel to the incident polarization while the other two beams show trivial effects. When the structural movement is aligned with polarization, the change in capacitance coupling between the fixed and the moveable beams induces around 30° phase differences between the two polarizations. The amplitude is not affected by the anisotropy and the insertion loss is less than 3 dB.

To dynamically control the polarization of THz wave, Zhao et al. demonstrated a tunable waveplate using pre-stressed microcantilever arrays, as illustrated in Figure 3f.[62] The tunable cantilevers are placed in the x-direction, providing phase retardation for quarter-wave plate (initial freestanding state) and half-wave plate (pull-in state), while the response from metamaterial is constant in y polarization. By applying 40 V bias, the pull-in microcantilever arrays shift the resonant frequency by around 230 GHz and convert the incident wave at 0.82 THz of 34° polarization angle from pure circular polarization to linear polarization. It also shows robustness against incident angles within 30°.

Manjappa et al. developed a reconfigurable SRR metamaterial in Figure 3g for logic operations with two electric inputs and a THz output.[63] The unit cell comprises of two SRRs laterally separated by a gap while beams of SRR are pre-stressed cantilevers, which are controlled separately as the two inputs. The far-field behaviors of Fano resonance exhibit exclusive-OR (XOR) and exclusive-NOR (XNOR) operations while the near-field electric field at the cantilever tips is measured as the NAND operation due to the resonant confinement.

Recently all-dielectric metamaterial and metasurface have attracted extensive attention as a solution for the intrinsic drawbacks of metals. However, such dielectric structures are not suitable for nanoelectromechanical tuning. Karvounis et al. reported a CMOS compatible electro-optic modulator in near-infrared based on freestanding ITO and Si bilayer nanowires, as shown in Figure 3h.[76] ITO is a low-index conductive material while Si is a high-index material, introducing antiparallel displacement currents in dimensionally asymmetric nanowire pairs. The actuation of the gap between two nanowires is achieved by the electrostriction property of bulk materials, where the small mechanical deformation rises from the quadratic coupling between strain and electric field and is dependent on the magnitude but not the polarity of the field. The modulation of transmission is up to 7% under a static bias of 2 V. At the natural mechanical resonant frequency of 6 MHz, it reaches 3.5% for a drive amplitude of 500 mV. The power consumption is only around 8 μW.

3. Metamaterials in Chemical Sensing Applications

3.1. Chemical Sensing Mechanisms

Metamaterials with strongly confined on-resonance electric and magnetic fields enable near-field couplings between radiations and molecule vibrations and therefore demonstrate promising potential in the ultrasensitive analysis of molecules. Such a near-field interaction involves both the refractive index (n) and the extinction coefficient (k) of the analyte and leads to the change in far-field behaviors. The frequency shift (Δf) of the metamaterial resonance is caused by the presence of the analyte which alters boundary conditions at the surface of the metamaterial and sensing medium. Transmittance or reflectance change of metamaterial resonance is caused by energy decay in the molecules and can be described by the absorption coefficient (α) or k. The molecular phonon resonance induces a significant change in n and k and further couples with the plasmonic resonance of metamaterial when their resonance frequencies are close to each other, which causes EIT, electromagnetically induced absorption (EIA), or Fano resonance depending on different coupling criteria.[66,109] Two types of metamaterial molecule sensors are defined as refractometry and surface enhanced spectroscopy according to their distinctive sensing mechanisms.

When half-wave dipole antenna is illuminated by linearly polarized EM wave, the oscillating electric field excites a surface current circulating within each plasmonic meta-atom at a specific frequency. This frequency is given by[110]

$$\lambda = \frac{2L}{m} n a_1 + a_2 \tag{2}$$

where L, m, n are the physical length of the antenna, model number, and refractive index of the surrounding medium, respectively. The constant a_2 accounts for the phase associated with the reflection at the antenna end, and the parameter a_1 depends on the antenna geometry and its material. From Equation (2), the resonance wavelength scales linearly with

antenna length L and n of the surrounding medium. In other words, for a metamaterial resonator with fixed length L, the resonance shift induced by the presence of refractive index from surrounding analyte can be measured to distinguish the molecules selectively, as the n and k in the target spectral range can be related to certain chemicals unambiguously. For the mixture of two substances such as solutes and solvents, the refractive index changes linearly with the concentration of solutes, which means the concentration of solutes can be quantified by monitoring the resonance shift. However, the refractive index is not a unique parameter of different molecules in a certain spectral range. It is possible that refractive indices are the same for two different molecules, which requires additional functionalization steps to perform selectivity. To distinguish various molecules, detecting vibration of chemical bonds inside molecules by surface enhanced spectroscopy is globally used because every molecule possesses a unique fingerprint absorption spectrum in the mid-IR and THz range.

The key to explaining the enhancement mechanism in resonant surface enhanced spectroscopy is the coupling between plasmonic vibration of metamaterial resonator and phonon vibration in molecules. The molecular vibration is only weakly excited via incident EM wave which is considered as a dark mode and the plasmonic vibration is strongly excited via incident EM wave which is considered as a bright mode. When bright mode resonance frequency is close to the dark mode resonance frequency, the coupling effect can result in EIT-like, EIA-like, or Fano-like line shape in far-field response. Many theory models are proposed to explain this phenomenon, such as modified functional forms of Fano-resonances,[111] coupled harmonic oscillators,[112] and TCMT.[66] Among them, TCMT provides further insights into Fano-resonant systems and reveals important parameters for an optimized design of metamaterial resonator used for surface enhanced spectroscopy. By leveraging two port coupling system, the reflectance of the metamaterial can be derived as

$$R(\omega)=\left|\frac{S_{1-}}{S_{1+}}\right|^2=\frac{\kappa^4}{(\omega-\omega_a)^2+(\gamma_{ae}+\gamma_{ao})^2} \tag{3}$$

where $\kappa=\sqrt{\gamma_{ae}}$ via reciprocity.[113,114] γ_{ae} and γ_{ao} are the external and internal losses, respectively. Equation (3) gives a Lorentzian line-shape whose amplitude and linewidth are determined by the relative contributions of the loss mechanisms. Furthermore, by inducing molecules into the coupling system, the reflectance can be derived as

$$R_{ab}=\frac{(\gamma_{ae})^2}{|D_{ab}|^2} \tag{4}$$

$$D_{ab}=\frac{|\mu|^2-(\omega-\omega_a)(\omega-\omega_b)+\gamma_a\gamma_{bo}+j[\gamma_a(\omega-\omega_b)+\gamma_{bo}(\omega-\omega_a)]}{j(\omega-\omega_b)+\gamma_{bo}} \tag{5}$$

where $\gamma_a=\gamma_{ae}+\gamma_{ao}$, and γ_{bo} is the damping rate of molecular resonance. μ, ω_a, ω_b are coupling rate of plasmon–phonon coupling and resonance frequency of plasmonic metamaterial and molecules, respectively. Depending on the matching of resonance frequency, the line shape of reflectance ranges from EIT-like dips ($\omega_a=\omega_b$) to Fano resonance ($\omega_a\neq\omega_b$). Similar results can also be calculated in transmittance. Additionally, using $A=1-T-R$, we can also derive the absorption as

$$A(\omega)=1-T-R=\frac{2\gamma_{ae}\gamma_{ao}}{(\omega-\omega_a)^2+(\gamma_{ae}+\gamma_{ao})^2} \tag{6}$$

Different line shapes of dips (EIT-like) and peaks (EIA-like) can be achieved depending on the ratio of γ_{ae} to γ_{ao}. By tracking the signature resonance frequency of molecules (ω_b) using enhancement of metamaterial resonator, the chemical vibration can be identified in mid-IR range while the vibration of the physical bond between molecules exists in the THz region. The coupling strength between metamaterial and molecules is affected by the near-field intensity of metamaterial resonators and the number of molecules inside the interaction area. Therefore, quantifying the concentration of chemicals is also workable using surface enhanced spectroscopy. The detection limit of molecule concentration is shown to be as low as sub-ppm level by the nanogap enhanced near-field.[115–121]

3.2. Metamaterials Chemical Sensing in IR

Mid-IR holds most of the molecular fingerprints and is emerging as a research area in molecular identification and dynamic monitoring. In addition to metamaterials, nanophotonics is another branch of research direction for mid-IR chemical sensing and functional applications,[122–125] which is beyond the scope of this review. Many works related to SEIRA have been done to detect analytes in the gas phase,[126–128] the solid phase (thin films),[129–136] and the liquid phase (solutions).[137–145]

Detection of gas pollutants like NO_x, SO_x, and breath metabolites like CO_2, the volatile organic compound (VOC) is significant in environment monitoring and personal healthcare. Gas sensors with miniaturized size, ultrahigh sensitivity, and fast response time remain a challenge hindered by the small size and the weak absorption of gas molecules. Leveraging resonant SEIRA in metamaterials, optical interaction length for the same detection resolution can be reduced by 1000 times compared to spiral waveguide[146] and free space nondispersive infrared (NDIR) gas sensor.[147] To further improve the detection limit of metamaterial gas sensors, different enrichment layers, such as graphene,[69] metal-organic framework (MOF),[148,149] polyethylenimine (PEI)[126,127] are used to trap gas molecules into metamaterial hotspots in order to locally enhance near-field interaction. Combining PEI and metamaterial absorber, Hasan et al. presented a hybrid metamaterial absorber for CO_2 sensing and achieved sub-ppm level resolution.[126] As shown in **Figure 4**a, the cross-shape hybrid metamaterial absorber made from Mo-AlN-Mo was spin-coated with PEI thin film and characterized in a heater-integrated gas chamber. There is a reversible chemical reaction between CO_2 and PEI so that additional fingerprints emerge from 6–8 μm and provide concentration information of CO_2. Additionally, physical absorption is another approach to trap gas molecules. Comparing to the chemical reaction, even though there is no identification selectivity in the physical trapping process, it can be used in multiple-gas sensor, where recognition can be achieved through unique absorption

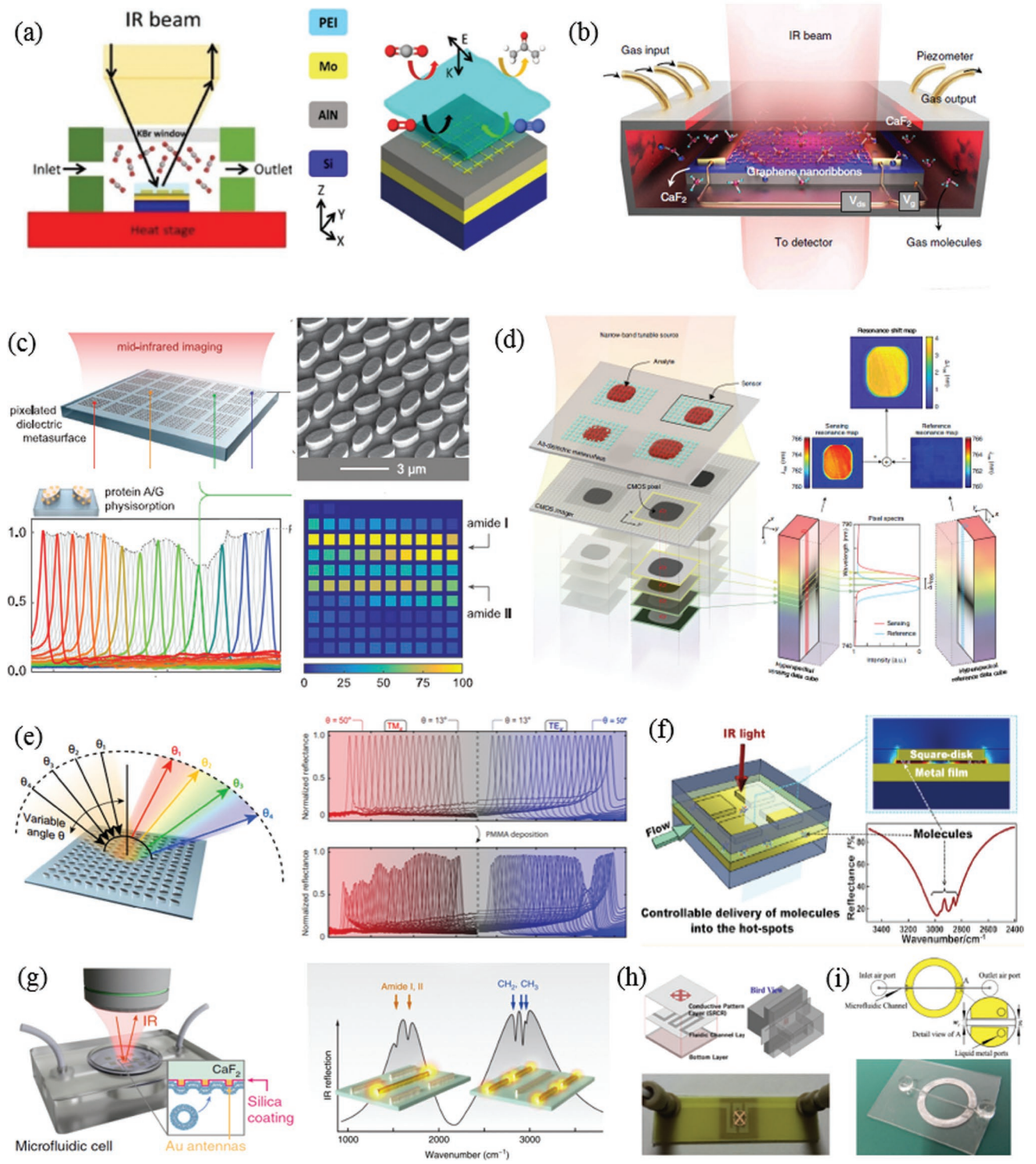

Figure 4. Metamaterial for chemical sensing application in IR and GHz. IR gas sensor using plasmonic metamaterial with gas enrichment layer of a) PEI and b) graphene; IR molecular imaging using multipixel metamaterial sensors by absorption fingerprints in c) mid-IR and d) wavelength shift in near-IR; e) Angle-multiplexed all-dielectric metasurfaces for broadband molecular fingerprint retrieval; liquid sensing in mid-IR using f) nanofluidic and g) microfluidic; h,i) microfluidic sensing in GHz region. (a) Reproduced with permission.[126] Copyright 2018, Wiley-VCH. (b) Reproduced with permission.[69] Copyright 2019, Springer Nature. (c) Reproduced with permission.[68] Copyright 2018, The American Association for the Advancement of Science. (d) Reproduced with permission.[164] Copyright 2019, Springer Nature. (e) Reproduced with permission.[165] Copyright 2019, The American Association for the Advancement of Science. (f) Reproduced with permission.[173] Copyright 2017, American Chemical Society. (g) Reproduced with permission.[145] Copyright 2018, Springer Nature. (h) Reproduced with permission.[186] Copyright 2016, Elsevier. (i) Reproduced with permission.[183] Copyright 2019, AIP Publishing.

fingerprints. As shown in Figure 4b, the graphene nanoribbon performs a multifunctional platform in gas sensing.[69] Through physisorption, N_2O, NO_2, and SO_2 are absorbed and accumulated into patterned graphene structure because of the polar nature of the molecules as well as the edge defect and dangling bonds in the graphene nanoribbons. The incident IR light excites the plasmons of graphene nanoribbons, and the resonant plasmons are coupled with trapped gas molecules. Real-time monitoring of incoming gas is achieved by tracking the reflectance change of signature absorption wavelength of each type of gas molecule. Thanks to the broadband resonance of graphene plasmons, the fingerprints of N_2O, NO_2, and SO_2 are simultaneously detected so that these gases can be distinguished in the mixture as well as in a dynamic process like a chemical reaction. Hybrid metamaterial platform consisting of plasmonic resonator and gas enrichment layer shows excellent advantages in gas identification and real-time dynamic monitoring. The combination of various absorption mechanisms needs to be developed and the resonant plasmonic structure needs to be optimized to further improve detection resolution to sub-ppb level. On the other hand, on-chip gas chamber integration will accelerate portable gas sensor applications in environmental monitoring and clinic diagnostics.

The thin films of poly-methyl methacrylate (PMMA)[136,150–153] and ODT[119,154,155] are the common analytes to characterize metamaterials sensing performance because they hold obvious fingerprints and are easy to functionalize on metamaterials resonator. During the last 10 years, many works were published utilizing various thin films of protein,[137,156] lipid,[157] DNA,[131,153,158–160] and other biomolecular analytes.[65,132,154,161–163] To overcome the limited detection of metamaterial resonators in the mid-IR fingerprint region, Tittl et al.[68] proposed a hyperspectral imaging system using all-dielectric metamaterial sensor array by varying the resonance wavelength of each sensor pixel, which enables bar-code identification of molecules. As shown in Figure 4c, the metamaterial sensor array covers a broadband IR wavelength range by designing a geometric size of each sensor pixel. Each sensor pixel works in a narrow bandwidth near its resonance wavelength and the data accumulated from all sensor pixels draw a clear picture of molecular fingerprint peaks in a broad wavelength range. Because of the unique fingerprint absorption for each type of molecule, a signature bar-code map is generated for identification. Besides, using linear regression, recognition of a mixture of two types of molecules from the bar-code image can also be achieved. The approach of leveraging image processing as the readout of the optical signal is also workable on refractometry sensing system. As shown in Figure 4d, Yesilkoy et al. proposed an integrated sensor system consisting of a monochromatic light source, metamaterial sensor array, and CMOS sensor array.[164] An algorithm is developed to convert transmittance intensity data to resonance vector so that the wavelength shift caused by the refractive index change of molecules is translated on the image. The fully integrated sensing system and powerful signal processing algorithm pave a way to a portable metamaterial sensor for real applications. In addition to fabricating sensor arrays with different dimensions, post-fabrication tuning is another approach to provide wavelength sweeping for molecular fingerprint retrieval. Li et al. proposed an active hybrid platform controlled by the graphene layer under the plasmonic antenna.[161] By applying voltage on the graphene sheet, the band structure of graphene is tuned and results in a wavelength shift of plasmonic nanoantenna from ≈6.4 to ≈7.2 μm, which matches the characteristic absorption of the amide bond in protein molecules. To realize the broad tuning range, Leitis et al. introduced a germanium-based metasurface sensor that combines chemically specific broadband IR detection with device-level simplicity and spectrometer-less operation of angle scanning refractometric approaches.[165] Through the different polarization states of TE_y and TM_x as well as the incident angle from 0° to 60° of incoming light, the quasi-bound states in the continuum (BIC) mode perform a tunable range from ≈5.5 to ≈9 μm. Figure 4e shows the experimental demonstration of this spectrometer-less angle-scanning molecular fingerprinting of broadband PMMA multiple absorption peaks.

Micro/nanofluidics is another interesting branch of metamaterial SEIRA bio-sensing application because most of the biomolecular processes happen in the aqueous environment.[140,166,167] Micro/nanofluidic chamber integrated on metamaterial sensors enable the transportation of micro/nanoliter scale biomolecular solutions to the hotspot of the sensing area at metasurface. The selectivity of desired biomolecules is activated after the surface functionalization of antibody on metamaterial sensors. However, the intrinsic absorption of water and other organic solvent hinder the operation mode of metamaterial biosensors. It is worth mentioning that most of the power will decay when the light transmits through the micrometer-thick water film in the THz and mid-IR regions. Some tricks need to be applied to fully leverage the advantages of metamaterials sensors integrated with micro/nanofluidics. In 2013, Adato et al. proposed a reflection-based plasmonic nanoantenna sensor on a CaF_2 substrate integrated with a PDMS microfluidic channel.[66] Thanks to the good transparency of CaF_2 glass at mid-IR wavelengths up to ≈8.5 μm, reflection signal can be detected to monitor the near-field interactions of nanoantennas and biomolecules. Based on this platform, real-time monitoring of in situ protein immunoassays via microfluidic integrated plasmonic metamaterial resonators was demonstrated. Following this sensing platform, Limaj et al. and Etezadi et al. achieved real-time monitoring of lipid membranes and protein secondary structure in 2016 and 2017, respectively.[137,157] As discussed above in Section 3.1, near-field enhancement is a key feature to improve the plasmon–phonon interaction, which will finally increase the sensitivity of plasmonic sensors. Many fundamental works have been done to improve the sensitivity of plasmonic sensors. One approach is to increase the near-field intensity by shrinking the gap between adjacent plasmonic nanoantennas to the nanometer scale,[121,168–172] the other way is to expose the hotspot area for the access of molecules which is blocked by the substrate.[119,154] However, there is a tradeoff between near-field intensity and hotspot area in planar metamaterial resonators. To further enhance sensitivity, the nanofluidic approach was presented by Le et al.[173] With the aid of the bottom gold mirror, quadrupolar resonance mode is excited in the metal-insulator-metal (MIM) structure, bringing a large area hotspot with an enhanced near-field intensity inside the nanometer-scale liquid chamber. As shown in Figure 4f, the analyte solution was filled in the hotspot generated by the nano-gapped MIM structure

with high near-field enhancement, which results in strong plasmon-phonon interaction. In addition, capillary effect inside MIM plasmonic nanogap structure is also studied to help deliver liquid analyte in sensing hotspot.[174] Since the characteristic fingerprint absorption peaks of different types of chemical bonds are separate in the mid-IR spectrum, multiband resonant structures are powerful for molecular identification by tracking diverse IR fingerprints.[175–179] From Figure 4g, a multi-resonant nanoantenna array integrated with microfluidics was used to monitor lipid membrane processes dynamically.[145] One resonance of multi-resonant antenna is located at ≈3 μm wavelength region sensing for O—H and C—H stretches, the other resonance is located at ≈6 μm wavelength region sensing for amide I and II. Comprehensive dynamic sensing of multiple fingerprints on different types of molecules was achieved, guided by the signal processing of mixture output using linear regression.

3.3. Metamaterials Chemical Sensing in GHz

In contrast to the IR spectral region, the GHz region with wavelength at the millimeter scale has also been explored for sensing applications. The larger feature size of metamaterial in the GHz spectral region allows easier fabrication and applications of sensors. More effective delivery of samples on sensing hotspot of each meta-atom can be achieved. Various chemical sensors have been reported with microfluidic channels through the sensitive gap region of each SRR meta-atom.[180–182] Arrays of SRR meta-atom with a fluidic channel passing through the gap region is also realized (Figure 4i).[183] In additional to SRR, chemical sensing can be achieved as well using the metamaterial absorber configuration.[184,185] The large feature size of metamaterial in the GHz region enables sensing at a specific hotspot of each meta-atom with various configurations (Figure 4h).[186,187] Sensing of a specific target molecule at hotspot was achieved through the selective functionalization of a molecule.[188] While IR and THz radiation can be largely absorbed by water samples, water absorption in the GHz region is significantly lower. Also, the larger feature size and longer wavelength of GHz radiation make it a candidate for the biological sensing of larger substances such as cells and tissues. The low absorption combined with a larger feature size of metamaterials may realize real-time biological studies of samples through the nondestructive electromagnetic wave.

3.4. Metamaterials Chemical Sensing in THz

Compared to the adjacent IR and GHz region, the THz radiation is less explored for sensing applications due to the lack of efficient sources, even though THz radiation is known for its low ionizing energy which causes less damage to target substances. THz is also a frequency region where many intra-molecular vibration modes exist. THz metamaterials may enhance the device sensitivity through the confinement of the electric and magnetic field at the sub-wavelength scale. MEMS technology is one of the ideal candidates to make sensitive devices. Many other functions can also be integrated onto a single chip such as sample preparation and post-processing functions. Besides, the advanced microfluidic techniques allow the handling of samples in the form of micro-droplet[189] or single cell[190] manipulation. In this section, THz metamaterials for sensing applications will be presented, and recent studies about the further combination of microfluidic technology will be discussed.

Thin film sensing has been reported through coating varied thicknesses of analyte on top of SRRs, which is the easiest way to deliver the molecular analytes on metasurface.[191] Kanamycin sulfate was dispersed on extraordinary optical transmission (EOT) metamaterial structure and dried in the air for sensing purposes.[192] Similarly, the complementary THz antenna was leveraged for 1,3,5-trinitroperhydro-1,3,5-triazine (RDX) sensing where the RDX molecule was dissolved in acetonitrile/methanol solutions in **Figure 5**a.[193] Signal enhancement up to 2800 times absorption cross section allows for a tiny quantity of molecule sensing near 40 ng. As shown in Figure 5b, THz slit antenna has also been used for sugar sensing by drying a certain amount of sugar-water solution droplets on top of the metasurface.[194] The antenna was designed at the molecular vibrational frequency of D-glucose and sucrose at ≈1.4 THz, and the change in the transmitted spectral response was observed. Sensing of larger bio-chemical molecules in the THz spectral region has also been reported. The deposition of bacteria layer with varied thickness was presented for detection.[195,196] In Figure 5c, virus[197] and yeast,[198,199] detection were also reported using metamaterial designed in the THz frequency region.

Despite several studies mentioned in the last paragraph about the detection of various types of biomolecules, it is essential to note that the samples were kept in dry conditions during the THz measurement. This is because water is highly absorptive to THz radiation, and thus the unique spectral response of biological samples in aqueous environment may be overwhelmed. However, water is an essential element in a biological system, and real-time observation of in vivo samples requires the measurement under aqueous environment. Hence, studies were conducted to overcome the water absorption issue to realize THz metamaterial sensor for practical applications. The integration of microfluidics and THz metamaterial has been reported as an effective method to overcome the water absorption issue. Microfluidics, confining liquid samples into a miniaturized micrometer-sized fluidic channel, enable precise manipulation of the target sample to metamaterials sensors and significantly reduce the amount of liquid sample exposed to THz radiation, which will reduce the influence of water absorption. Lying in between the nanometer scale IR region and the millimeter scale GHz region, metamaterial in the THz region is the ideal candidate for integration with the microfluidic technology which has been developed in the micrometer scale. However, compared to adjacent IR and GHz spectral region, only a few THz microfluidic metamaterial sensing have been studied. An earlier report has encapsulated the metamaterial Si chip into a fluidic chamber for the detection of bovine serum albumin (BSA) solution.[200] The soft lithography process using PDMS has been utilized for microfluidic metamaterial chips where the whole metamaterial surface is covered by a PDMS fluidic chamber. This method has been reported for sensing of alcoholic solution[201] (Figure 5d) and biomarker[202] (Figure 5e).

The confinement of the target sample at the hotspot of each meta-atom and integration with nanofluidic techniques can be further studied. This can be done through site-selective

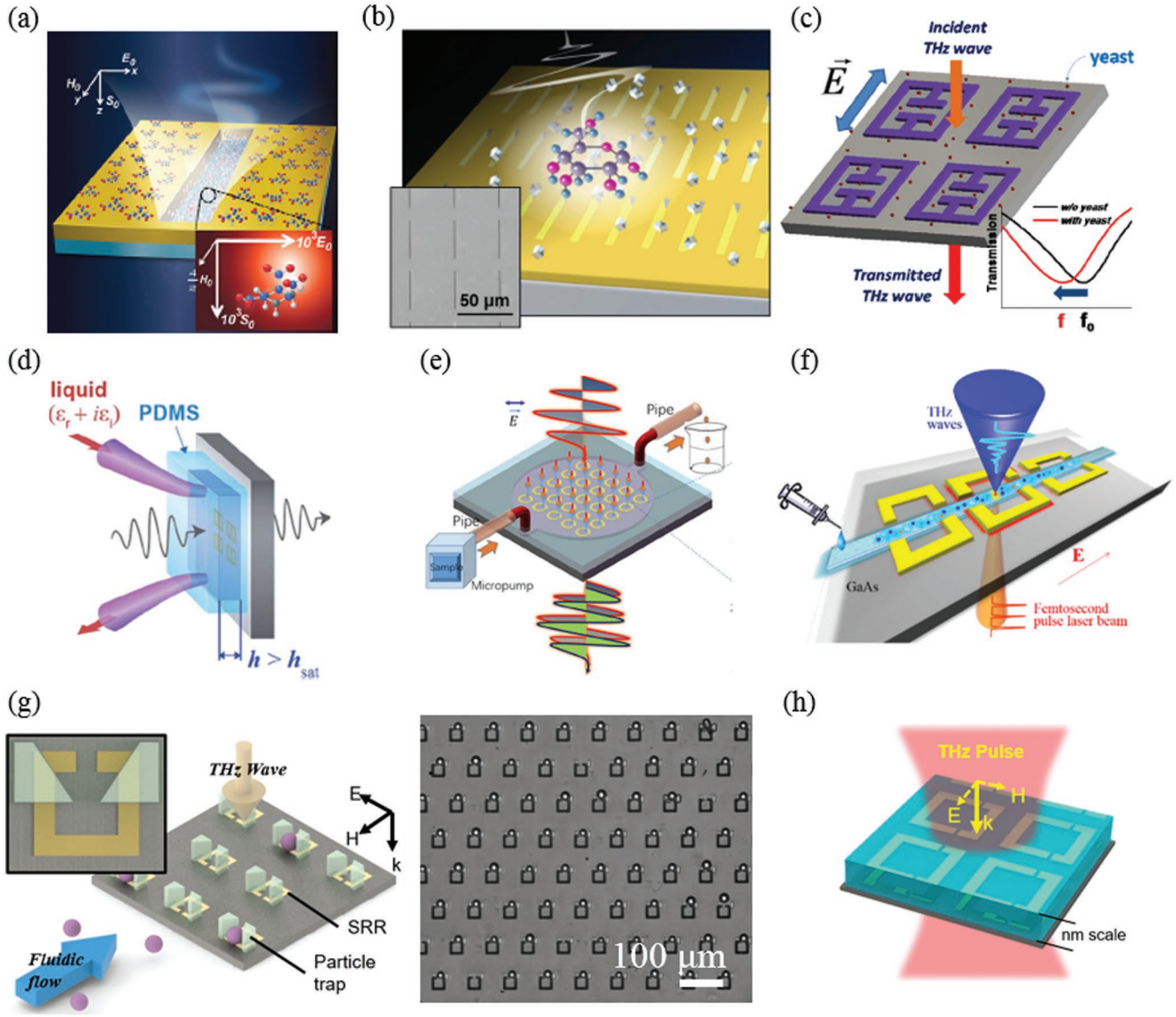

Figure 5. Metamaterial for chemical sensing application in THz. a) RDX, b) sugars, and c) yeast sensors. THz metamaterial sensor; microfluidics metamaterial d) chemical sensor and e) biomarker sensor, f) sensing of chemicals at SRR sensitive gap; g) selective trapping of microparticle at SRR hotspot; h) nanofluidic ATP sensing. (a) Reproduced with permission.[193] Copyright 2013, American Chemical Society. (b) Reproduced with permission.[198] Copyright 2015, Springer Nature. (c) Reproduced with permission.[198] Copyright 2017, IOP Publishing. (d) Reproduced with permission.[201] Copyright 2016, RSC Publishing. (e) Reproduced with permission.[202] Copyright 2017, Springer Nature. (f) Reproduced with permission.[204] Copyright 2018, AIP Publishing. (g) Reproduced with permission.[183] Copyright 2017, AIP Publishing. (h) Reproduced with permission.[185] Copyright 2018, AIP Publishing.

functionalization of self-assembled monolayer for a target molecule, or through integrating microfluidic trapping structures with each meta-atom. Recently, selective trapping of microparticle at sensitive hot-spot of each metamaterial unit cell has been reported.[203] As shown in Figure 5g, microparticles are trapped at the sensitive gap of SRR by SU-8 trapping structure fabricated inside the microfluidic channel. Only one particle is being trapped at each single meta-atom. Selective sensing of chemicals at metamaterial hotspot has also been reported. Instead of covering the whole metasurface with the fluidic chamber, the chemical sensor with liquid only flowing through sensitive hotspot has also been demonstrated in Figure 5f.[204] The most effective way to diminish the water absorption is to reduce the optical interaction length, which is the thickness of the microfluidic system. Therefore, the nanofluidic platform is developed for THz sensing in the aqueous environment. In Figure 5h, selective sensing of adenosine triphosphate (ATP) was demonstrated through aptamer functionalization on Au metallic metamaterial patterns, which allows in vivo monitoring of bioprocess in the aqueous environment.[205]

4. Metamaterials Enhanced Physical Sensors

The integration of MEMS with metamaterials is employed to not only construct tunable metamaterials but also realize

high-performance physical sensors, especially IR and THz radiation detectors. There are mainly two approaches to the implementation of radiation detectors: one is the photon detector, the other is the thermal detector. When radiation occurs, photon detectors exploit photogenerated carriers. Therefore, they typically require cryogenic cooling to suppress thermally generated carriers, which is considered as a noise in the system. Alternatively, thermal detectors utilize changes in material properties induced by temperature variation. As a result, they are free from cooling assistance, making themselves more compact, more efficient, and less expensive. MEMS technology has been employed to design uncooled radiation detectors with miniaturized footprint and high sensitivity, such as microbolometer and thermopile.[206–208] However, the drawbacks of conventional uncooled MEMS radiation detectors are inefficient absorption and a lack of wavelength selectivity. To overcome this limitation, plasmonic metamaterial absorbers are integrated with MEMS detectors to enhance absorption and realize wavelength selectivity.[209] Based on such hybrid platforms, uncooled radiation detectors consisting of metamaterial absorber attached to conventional microbolometer and thermopile have been demonstrated,[70,210] showing enhanced responsivity at designed wavelengths.

In terms of the MEMS sensor mechanisms, the one based on resonator offers unique advantages over the above-mentioned nonresonant structures, including high sensitivity enabled by reduced footprint and low noise (as a result of high resolution) thanks to the intrinsic high Q factor. Furthermore, the frequency output of resonant sensors can be measured more accurately than other physical quantities such as voltage and current. Hui et al. from the group of Prof. M. Rinaldi at Northeastern University demonstrated a plasmonically enhanced piezoelectric MEMS resonant infrared detector (**Figure 6**a).[73] The resonator is composed of a top gold plasmonic metasurface, a middle AlN piezoelectric nanoplate, and the bottom platinum interdigitated transducer. The plasmonic absorber selectively absorbs incident IR radiation at 8.8 μm, which is determined by unit cell dimensions. As a result, the resonator is

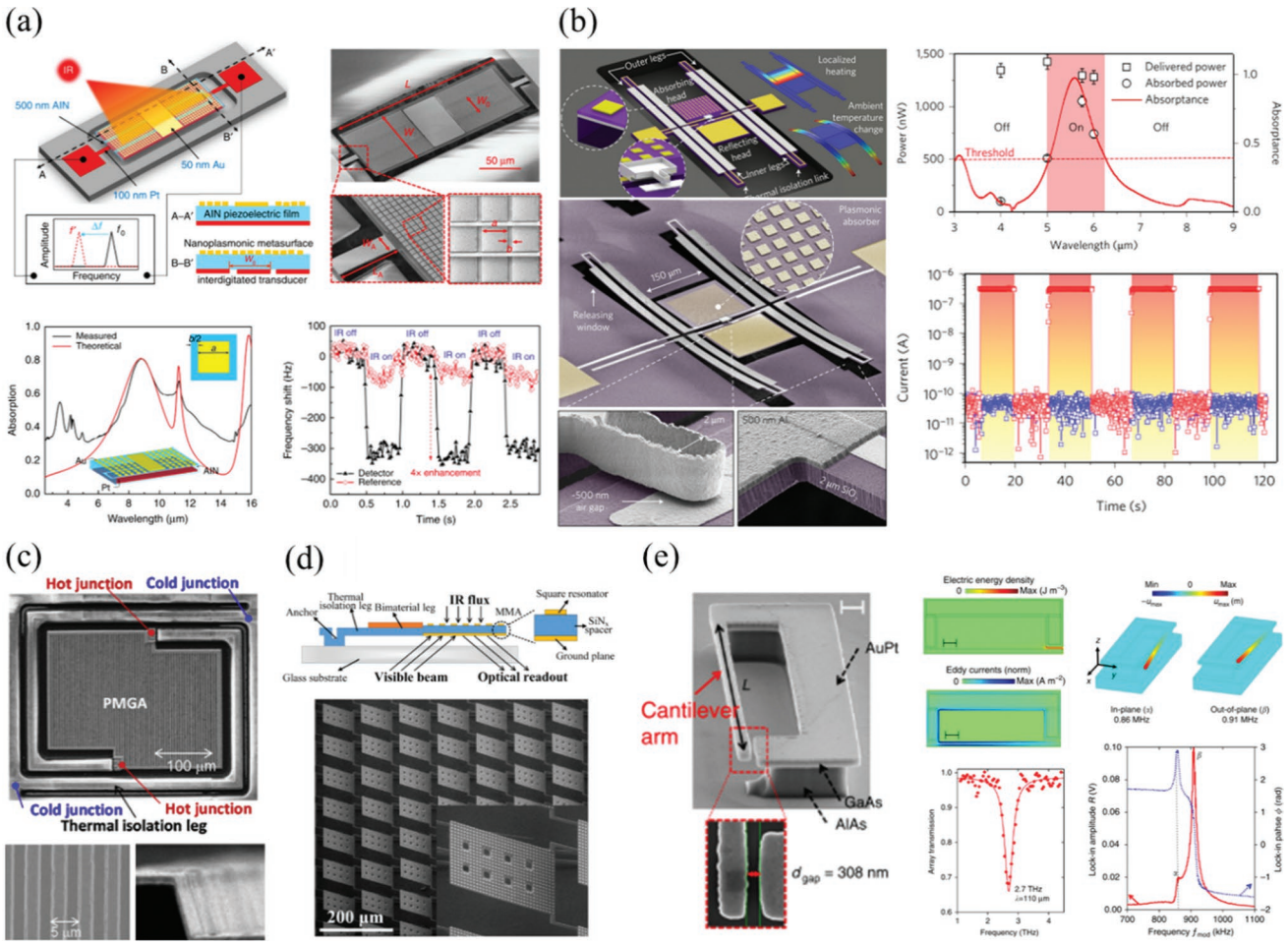

Figure 6. Metamaterials for physical sensing application. a) Plasmonically enhanced piezoelectric MEMS resonant infrared detector. b) Zero-power digitized infrared detector based on plasmonically enhanced MEMS thermal photoswitch. c) Broadband polarization-selective MEMS thermopile infrared sensor using plasmonic grating absorber. d) Metamaterial enhanced MEMS thermal bimaterial cantilever infrared focal plane array. e) Optomechanical terahertz detector based on SRR with MEMS cantilever. (a) Reproduced with permission.[73] Copyright 2016, Springer Nature. (b) Reproduced with permission.[75] Copyright 2017, Springer Nature. (c) Reproduced with permission.[212] Copyright 2017, Elsevier. (d) Reproduced with permission.[72] Copyright 2015, AIP Publishing. (e) Reproduced with permission.[74] Copyright 2017, Springer Nature.

heated up and its resonant frequency is shifted. The plasmonic piezoelectric resonator shows fourfold enhanced responsivity compared with its counterpart without plasmonic absorber.

Afterward, Qian et al. developed a zero-power digitized infrared detector based on plasmonically enhanced MEMS thermal photoswitch (PMP) (Figure 6b).[75] The PMP is composed of two identical cantilevers face-to-face. Each cantilever is made up of a head, an inner pair of bimaterial legs for actuation, and an outer pair of identical bimaterial legs for compensation, which are connected by a pair of thermal isolation links. The head of one cantilever is integrated with a plasmonic IR absorber and a metal tip electrically connected to one of the device terminals. The absorbed IR radiation increases the temperature, and thus bends the actuation legs downward, bringing the metal tip into contact with the opposite terminal when the absorbed radiation power exceeds the designed threshold. Thanks to the built-in compensation mechanism, the inner and outer pairs of bimaterial legs bend in the same direction with nearly identical displacement in response to ambient temperature change and residual stress, which preserves the designed gap between the device contacts. A PMP with a designed triggering spectral band centered at ≈5.6 μm was fabricated. The PMP was turned on when illuminated by in-band infrared radiation at 5, 5.75, and 6 μm, whereas it remained in the off-state with incident off-band infrared radiation at 4 μm. The measured current through the PMP (red lines) in response to chopped infrared radiation at 5 μm (red shadow) clearly indicates reversible digitized on-off switching. This work opens a new path to construct radiation sensors.

In addition to wavelength selectivity, plasmonic metamaterial absorbers can also introduce polarization selectivity to conventional MEMS thermal radiation detectors. Polarization selectivity can be achieved by adding a symmetry-breaking structure to the two in-plane orthogonal directions. Ogawa et al. proposed a polarization-selective thermopile IR sensor through changing the dimple shape of the plasmonic absorber from circle to ellipse.[211] Such asymmetric 2D plasmonic absorber shows sufficient absorption when the electric field of the incident radiation is perpendicular to the major axis of the elliptical dimple, while it does not absorb incident radiation with its electric field parallel to the major axis. The author also demonstrated another approach by replacing 2D periodic dimples with 1D gratings (Figure 6c).[212] In addition to polarization selectivity, broadband absorption was realized by increasing the grating depth. Multi-wavelength plasmonic resonances occurring in both in-plane and out-of-plane directions produced broadband absorption. As a result, broadband polarization selectivity was achieved.

The integration of metamaterial absorbers and MEMS radiation detectors have also been employed to form focal plane arrays (FPAs) in both THz and IR ranges. Tao et al. demonstrated the first metamaterial enhanced THz FPA.[71] Every detection pixel is comprised of an SRR, a bimaterial cantilever, and an optically reflective pad. The SRRs absorb the incident THz radiation and convert it to heat, resulting in the deformation of the bimaterial cantilevers. This mechanical deflection is read out by optical interrogation of the reflective pads using visible light. Using this FPA, the capture of a THz beam profile was demonstrated. Ma et al. utilized a similar idea and demonstrated metamaterial enhanced FPA in the IR range (Figure 6d).[72] Rather than SRR, MIM-type metamaterial absorber was used, which consists of gold squared resonators, SiN_x structural layer, and a gold ground plane. The ground plane also performs as the mirror for reverse optical readout configuration. The image of human body captured by the FPA integrated with metamaterial absorber possesses higher grayscale value and clearer profile than that captured by the FPA without metamaterial absorber.

The interaction between EM waves and metamaterials not only leads to photothermal effect but also generates near-field optical forces, which also can be utilized for EM wave detection. Belacel et al. developed a new platform for THz detection using both effects (Figure 6e).[74] The device consists of an asymmetric SRR with a suspended MEMS cantilever. When the device is illuminated by THz radiation, the SRR is excited in resonance and the electric energy is confined in the gap. As a result, a Coulomb force is generated and attracts the cantilever toward the opposite side of the gap, activating the in-plane (α) mechanical resonance mode. Conversely, the out-of-plane (β) mode is dominated by the photothermal force originating from the bimaterial structure of the cantilever. Quantum cascade laser is used as a THz source to excite SRR resonance with a modulation frequency f_{mod}. The mechanical response of the SRR was obtained by sweeping f_{mod} and recorded by the lock-in amplifier connected to the photodetector. Unlike photothermal force, Coulomb force is not limited by the thermal diffusion time constant. The noise equivalent power of the detection mechanism based on the Coulomb interaction is independent of the mechanical frequency. Moreover, the compact geometry of the device enables uncooled radiation detection with extremely short thermal diffusion time, on the order of few microseconds.

It is also worth noting that the mechanical deformation of metamaterials by photothermal force and near-field optical forces can realize optically reconfigurable metamaterials, which perform intensity-dependent (i.e., nonlinear) response. Ou et al. from the group of Prof. N. I. Zheludev demonstrated plasmonic metamaterials patterned on MEMS actuators with significant nonlinearity.[213] Nonlinear metamaterials possess significantly enhanced nonlinearity as compared to natural materials and thus promising potential in many applications such as harmonic generation and parametric amplification.[214]

5. 3D Metamaterials

As discussed in Sections 2–4, the combination of MEMS and metamaterials technology shows advances in the diversified optical application. However, due to the limitation of traditional CMOS nano-fabrication process, most of the metamaterial devices are limited to planar structure or multilayer planar structure. Therefore, expanding 2D metasurface to 3D metamaterials structure will bring more possibility to enhance EM properties such as novel resonance modes and giant optical chirality, which paves the way to the advanced optical application of meta-devices.[215–223] Comparing to 3D structures in the macroscopy domain, it is still difficult to construct nanostructure in 3D space. Therefore, many research efforts have been

conducted to develop fabrication techniques for 3D nanostructure such as membrane projection lithography (MPL),[224,225] self-folding origami,[226] self-assembly,[227] nano-transfer printing,[228] and nano-kirigami.[229]

Among those approaches, MPL is first studied to form 3D meta-atom. As shown in **Figure 7**a, Burchel et al. developed an MPL process using a suspended membrane to transfer the pattern to different sides of the bottom walls by tilting the deposition angle.[224] In this work, SU-8 with a thickness of the final unit cell height forms the bottom walls and polyimide is deposited as sacrificial to suspend the membrane. After top PMMA layer is patterned, polyimide sacrificial layer is removed by tri-methyl ammonium hydroxide (TMAH) resist developer. After metal deposition for five times and the following lift-off process, the 3D meta-atom with 5 SRR on both walls and substrates is fabricated, and the SEM image is shown in Figure 7a. The orientation of SRR on different sides of the SU-8 walls is different because of the projection image difference of membrane. Therefore, the 3D meta-atom can be decomposed into three electrically coupled SRRs and two magnetically coupled SRRs, which each responds to orthogonal polarizations. Figure 7a shows the experiment results of the 3D metamaterials, which prove the decomposition of five SRRs.

Due to the asymmetry of the projection image, MPL can only fabricate the 3D structures in a specific orientation limited

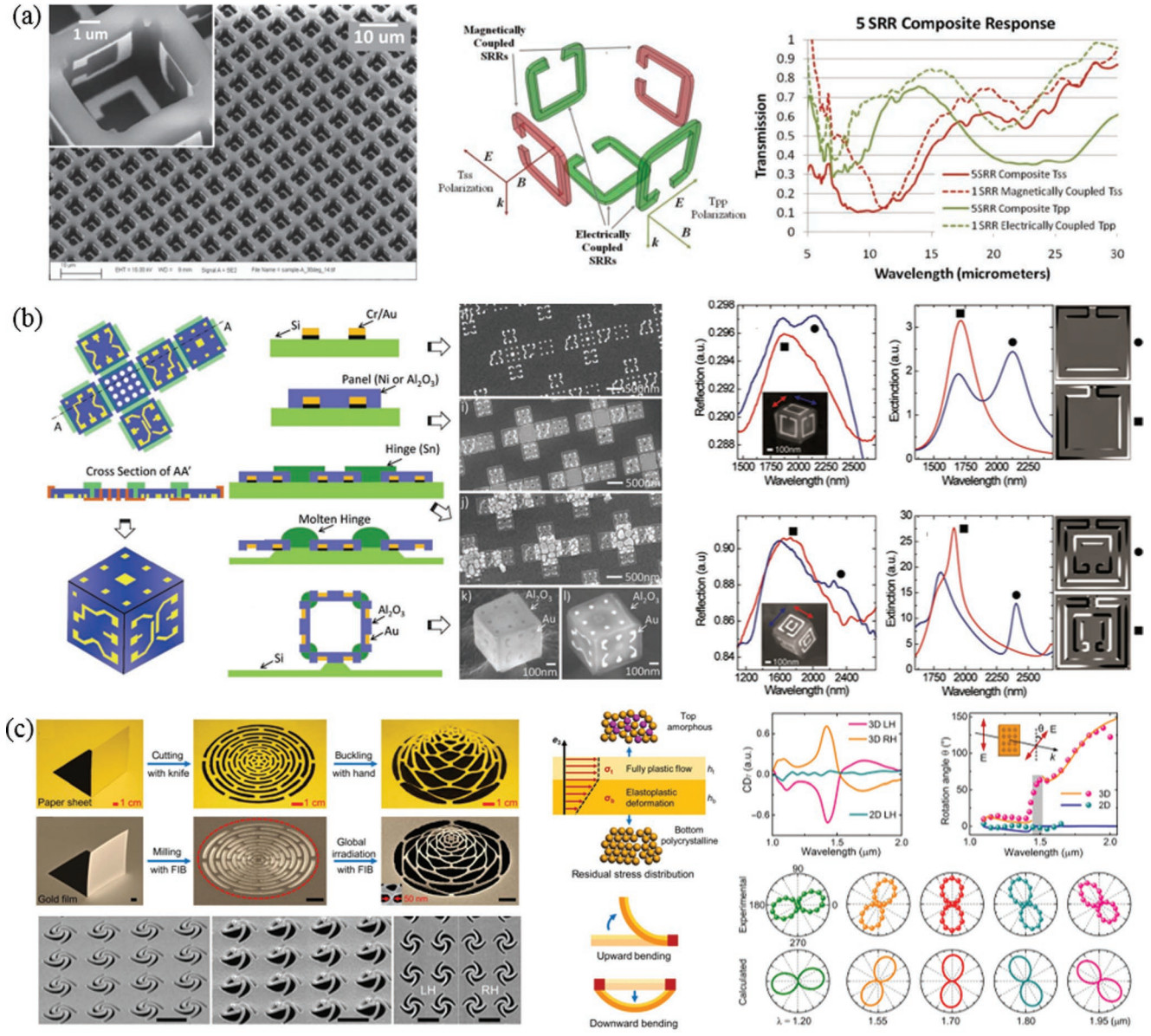

Figure 7. Fabrication methods and characterization of 3D metamaterials. a) MPL process and five SRRs composite response; b) self-folding origami and experimental observation of high-order mode. c) Nano-kirigami with enhanced optical chirality. (a) Reproduced with permission.[224] Copyright 2010, Wiley-VCH. (b) Reproduced with permission.[226] Copyright 2011, Wiley-VCH. (c) Reproduced with permission.[229] Copyright 2018, The American Association for the Advancement of Science.

by the projection on the membrane. To overcome this limitation, Cho et al. develop a nanoscale origami process to fabricate 3D metamaterials.[226] Inspired by the ancient Japanese art of paper folding—Origami, they transfer the 2D flat sheets to 3D structures. As shown in Figure 7b, the pattern is first defined by the lift-off process, following by the formation of panels and hinges. To achieve the origami-type folding, plasma etching is conducted to undercut the underlying Si substrate. During etching, the heat generated by the exothermic etching process causes grain coalescence or reflow of the Sn hinges, which act as self-folds by making a torque to rotate panels and create the 3D nanostructure. Moreover, 3D nanostructure with the plasmonic resonator on each surface provides an advanced platform for biochemical sensing application. As discussed in Section 4, plasmonic resonance with high Q factor and low loss provides molecular sensing with high sensitivity. However, it is difficult to excite such high order low-loss narrow resonances in 2D planar metasurfaces due to momentum mismatch. As Figure 7b illustrates, cross-shaped plasmonic resonators on the side faces of the 3D nanocube will easily be excited at their quadrupole plasmon mode due to phase retardation of the normal incident light.

In addition to achieving novel resonance modes, 3D metamaterials are also beneficial to perform giant optical chirality.[227,229] Inspired by the art of paper-cut, Liu et al. utilized nano-kirigami to make 3D metamaterial structure, which is demonstrated in Figure 7c. By applying gallium (Ga) ion collision to suspended gold structure, strong physical bombardment will introduce Ga dopant on the top gold surface, which will further induce the residual stress. Depending on the mechanical structure, upward bending and downward bending will occur on the cantilever and fixed-fixed beam structure, respectively. Based on this technology, 3D pinwheel metamaterial is fabricated and characterized, which is illustrated in Figure 7c. Compared with 2D planar metasurface, 3D pinwheel structure significantly enhances the optical chirality by simply inducing 3D twisted structure through nano-kirigami.

Besides, active tuning of 3D metamaterials is also achieved using the origami structure.[230–232] In 2012, Fuchi et al. propose a tunable origami metamaterial working at GHz region. By tuning the folding angle of 3D structure, resonance peaks at a different frequency can be observed. Later in 2014, reconfigurable 3D plasmonic meta-molecules are demonstrated to execute DNA-regulated conformational changes at the nanoscale.[230] DNA serves as both a construction material to organize plasmonic nanoparticles in three dimensions, as well as fuel for driving the meta-molecules to distinct conformational states. Simultaneously, the 3D plasmonic meta-molecules can work as optical reporters, which transduce their conformational changes in situ into circular dichroism changes in the visible wavelength range. In 2017, Wang et al. reported origami-based metamaterials whose electromagnetic responses are dynamically controllable via switching the folding state of Miura-Ori SRRs.[232] The deformation of the Miura-Ori unit along the third dimension induces net electric and magnetic dipoles of SRR that is parallel or anti-parallel to each other, leading to the strong chiral responses. Circular dichroism as high as 0.6 is experimentally observed while the chirality switching is realized by controlling the deformation direction and kinematics.

6. Conclusion and Outlook

Metamaterial devices leveraging MEMS and micro/nanofluidic have grown in scientific and technological relevance from a fundamental effect to practical applications. Micro/nanoscale manipulation of metamaterials shows significant advances in functional EM devices, surface enhanced chemical sensing, and wavelength-selective radiation detection. In MEMS tunable metamaterial devices, various types of MEMS actuators, for example, thermal actuator, piezoelectric actuator, electrostatic actuator, etc., have been used to modulate metamaterial resonance frequency, amplitude, as well as phase, which brings to advanced application in optical switch, logic operation, wavelength tunable and polarization selective absorber, tunable slow light effect, tunable waveplate, and so on. Besides, by integrating micro/nanofluidics or gas enrichment layer with metamaterial resonators, it boosts surface enhanced chemical sensing, which allows real-time in situ monitoring of the biomolecular process with high sensitivity and selectivity, as well as molecular identification in IR and THz regions. As reported, plasmonic metamaterial absorbers have been applied to MEMS radiation detectors and zero-power devices based on various mechanisms. A significant improvement in the radiation absorption coefficient was achieved. Leveraging the delicate design of MEMS actuators, functional metamaterial responses such as digitized and nonlinear responses can be realized, laying a foundation for on-chip signal processing. Moreover, 3D metamaterials with enhanced optical characteristics like novel resonance mode and giant chirality will reinforce the applications in functional devices, chemical sensors, and physical sensors.

In conclusion, with the rapid development of relevant science and technology in recent years, MEMS and micro/nanofluidics have been developed toward a standard technology platform to achieve basic tunability and advanced application of metamaterial devices. In the future, for MEMS functional devices, the challenge remains to shrink moveable structure to the nanometer scale to achieve nano-micromechanical systems (NEMS), which will extend the working frequency range of MEMS tunable metamaterial to IR and visible spectrum. For surface enhanced chemical sensing, the prospect will be further increasing detection sensitivity and detection bandwidth by optimizing metamaterial structures. Future efforts in the integration of metamaterial with MEMS, specifically for radiation detection, could be the integration of MEMS metamaterials with different designs, to realize multi-functional sensing and signal processing platform. 3D metamaterial with advanced optical properties still needs to be further developed to perform diversified optical applications. All in all, the combination of functional devices, chemical sensors, physical sensors together with other accessories to construct smart-sensor microsystem enables powerful applications in booming healthcare, environmental monitoring, and IoT regions.

Acknowledgements

Z.R., Y.C., Y.M. contributed equally to this work. This work was sponsored by the research grant of NRF-CRP15-2015-02 "Piezoelectric Photonics Using CMOS Compatible AlN Technology for Enabling The Next Generation Photonics ICs and Nanosensors" at the National University

of Singapore (NUS), Singapore; the research grant of NRF2015-NRF-ISF001-2620 "Reconfigurable data center optical interconnects using fast nanophotonic MEMS waveguide switches" at the NUS, Singapore; the research grant of RIE Advanced Manufacturing and Engineering (AME) programmatic grant A18A5b0056 "BRain-Efficient Nanomechanical Artificial Intelligence Computing (BRENAIC)" at NUS, Singapore; and the research grant of RIE Advanced Manufacturing and Engineering (AME) programmatic grant A18A4b0055 "Nanosystems at the Edge" at NUS, Singapore.

Conflict of Interest

The authors declare no conflict of interest.

Keywords

infrared detectors, metamaterials, micro/nanofluidics, microelectro-mechanical system, terahertz devices

Received: April 19, 2019
Revised: June 10, 2019
Published online:

[1] S. Linden, C. Enkrich, M. Wegener, J. Zhou, T. Koschny, C. M. Soukoulis, *Science* **2004**, *306*, 1351.
[2] T. J. Yen, W. Padilla, N. Fang, D. C. Vier, D. R. Smith, J. B. Pendry, D. N. Basov, X. Zhang, *Science* **2004**, *303*, 1494.
[3] S. Xiao, V. P. Drachev, A. V. Kildishev, X. Ni, U. K. Chettiar, H. K. Yuan, V. M. Shalaev, *Nature* **2010**, *466*, 735.
[4] C. M. Soukoulis, S. Linden, M. Wegener, *Science* **2007**, *315*, 47.
[5] W. J. Padilla, D. N. Basov, D. R. Smith, *Mater. Today* **2006**, *9*, 28.
[6] D. R. Smith, J. B. Pendry, M. C. K. Wiltshire, *Science* **2004**, *305*, 788.
[7] R. A. Shelby, D. R. Smith, S. Schultz, *Science* **2001**, *292*, 77.
[8] K. Chen, Y. Feng, F. Monticone, J. Zhao, B. Zhu, T. Jiang, L. Zhang, Y. Kim, X. Ding, S. Zhang, A. Alù, C. W. Qiu, *Adv. Mater.* **2017**, *29*, 1606422.
[9] X. Chen, L. Huang, H. Mühlenbernd, G. Li, B. Bai, Q. Tan, G. Jin, C. W. Qiu, S. Zhang, T. Zentgraf, *Nat. Commun.* **2012**, *3*, 1198.
[10] W. T. Chen, A. Y. Zhu, V. Sanjeev, M. Khorasaninejad, Z. Shi, E. Lee, F. Capasso, *Nat. Nanotechnol.* **2018**, *13*, 220.
[11] Z. Jacob, L. V. Alekseyev, E. Narimanov, in *Conf. Quantum Electron. Laser Sci. (CLEO/QELS 2007) – Tech. Dig. Ser.*, **2007**, p. 2095.
[12] S. Wang, P. C. Wu, V. C. Su, Y. C. Lai, M. K. Chen, H. Y. Kuo, B. H. Chen, Y. H. Chen, T. T. Huang, J. H. Wang, R. M. Lin, C. H. Kuan, T. Li, Z. Wang, S. Zhu, D. P. Tsai, *Nat. Nanotechnol.* **2018**, *13*, 227.
[13] N. Fang, H. Lee, C. Sun, X. Zhang, *Science* **2005**, *308*, 534.
[14] H. Tao, C. M. Bingham, A. C. Strikwerda, D. Pilon, D. Shrekenhamer, N. I. Landy, K. Fan, X. Zhang, W. J. Padilla, R. D. Averitt, *Phys. Rev. B* **2008**, *78*, 241103.
[15] C. Wu, B. Neuner, G. Shvets, J. John, A. Milder, B. Zollars, S. Savoy, *Phys. Rev. B* **2011**, *84*, 075102.
[16] A. Andryieuski, A. V. Lavrinenko, *Opt. Express* **2013**, *21*, 9144.
[17] D. Shrekenhamer, W. C. Chen, W. J. Padilla, *Phys. Rev. Lett.* **2013**, *110*, 177403.
[18] C. M. Watts, X. Liu, W. J. Padilla, *Adv. Mater.* **2012**, *24*, 98.
[19] X. Liu, T. Starr, A. F. Starr, W. J. Padilla, *Phys. Rev. Lett.* **2010**, *104*, 207403.
[20] M. K. Hedayati, F. Faupel, M. Elbahri, *Materials* **2014**, *7*, 1221.
[21] N. I. Landy, S. Sajuyigbe, J. J. Mock, D. R. Smith, W. J. Padilla, *Phys. Rev. Lett.* **2008**, *100*, 207402.
[22] S. Y. Chiam, R. Singh, C. Rockstuhl, F. Lederer, W. Zhang, A. A. Bettiol, *Phys. Rev. B* **2009**, *80*, 153103.
[23] J. Gu, R. Singh, X. Liu, X. Zhang, Y. Ma, S. Zhang, S. A. Maier, Z. Tian, A. K. Azad, H. T. Chen, A. J. Taylor, J. Han, W. Zhang, *Nat. Commun.* **2012**, *3*, 1151.
[24] N. Liu, L. Langguth, T. Weiss, J. Kästel, M. Fleischhauer, T. Pfau, H. Giessen, *Nat. Mater.* **2009**, *8*, 758.
[25] P. Tassin, L. Zhang, T. Koschny, E. N. Economou, C. M. Soukoulis, *Phys. Rev. Lett.* **2009**, *102*, 053901.
[26] S. Zhang, D. A. Genov, Y. Wang, M. Liu, X. Zhang, *Phys. Rev. Lett.* **2008**, *101*, 047401.
[27] J. Hua, M. L. Chen, L. Zhu, F. Y. Meng, Q. Wu, in *Proc. 2012 5th Global Symp. Millimeter-Waves (GSMM 2012)*, **2012**, https://doi.org/10.1109/GSMM.2012.6314089.
[28] M. Choi, S. H. Lee, Y. Kim, S. B. Kang, J. Shin, M. H. Kwak, K. Y. Kang, Y. H. Lee, N. Park, B. Min, *Nature* **2011**, *470*, 369.
[29] E. Plum, V. A. Fedotov, N. I. Zheludev, *Appl. Phys. Lett.* **2008**, *93*, 191911.
[30] W. Panpradit, A. Sonsilphong, C. Soemphol, N. Wongkasem, *J. Opt.* **2012**, *14*, 075101.
[31] B. Wang, J. Zhou, T. Koschny, C. M. Soukoulis, *Appl. Phys. Lett.* **2009**, *94*, 151112.
[32] E. Plum, J. Zhou, J. Dong, V. A. Fedotov, T. Koschny, C. M. Soukoulis, N. I. Zheludev, *Phys. Rev. B* **2009**, *79*, 035047.
[33] W. J. Padilla, A. J. Taylor, C. Highstrete, M. Lee, R. D. Averitt, *Phys. Rev. Lett.* **2006**, *96*, 107401.
[34] H. T. Chen, J. F. O'Hara, A. K. Azad, A. J. Taylor, R. D. Averitt, D. B. Shrekenhamer, W. J. Padilla, *Nat. Photonics* **2008**, *2*, 295.
[35] Z. Liu, C.-Y. Huang, H. Liu, X. Zhang, C. Lee, *Opt. Express* **2013**, *21*, 6519.
[36] S. Savo, D. Shrekenhamer, W. J. Padilla, *Adv. Opt. Mater.* **2014**, *2*, 275.
[37] D. Shrekenhamer, S. Rout, A. C. Strikwerda, C. Bingham, R. D. Averitt, S. Sonkusale, W. J. Padilla, *Opt. Express* **2011**, *19*, 9968.
[38] O. Paul, C. Imhof, B. Lägel, S. Wolff, J. Heinrich, S. Höfling, A. Forchel, R. Zengerle, R. Beigang, M. Rahm, *Opt. Express* **2009**, *17*, 819.
[39] A. Benz, I. Montaño, J. F. Klem, I. Brener, *Appl. Phys. Lett.* **2013**, *103*, 263116.
[40] H.-T. Chen, W. J. Padilla, J. M. O. Zide, A. C. Gossard, A. J. Taylor, R. D. Averitt, *Nature* **2006**, *444*, 597.
[41] N. Chen, D. Hasan, C. P. Ho, C. Lee, *Adv. Mater. Technol.* **2018**, *3*, 1800014.
[42] L. Ju, B. Geng, J. Horng, C. Girit, M. Martin, Z. Hao, H. A. Bechtel, X. Liang, A. Zettl, Y. R. Shen, F. Wang, *Nat. Nanotechnol.* **2011**, *6*, 630.
[43] S. H. Lee, M. Choi, T. T. Kim, S. Lee, M. Liu, X. Yin, H. K. Choi, S. S. Lee, C. G. Choi, S. Y. Choi, X. Zhang, B. Min, *Nat. Mater.* **2012**, *11*, 936.
[44] H. Němec, P. Kužel, F. Kadlec, C. Kadlec, R. Yahiaoui, P. Mounaix, *Phys. Rev. B* **2009**, *79*, 2.
[45] R. Singh, A. K. Azad, Q. X. Jia, A. J. Taylor, H.-T. Chen, *Opt. Lett.* **2011**, *36*, 1230.
[46] M. A. Kats, D. Sharma, J. Lin, P. Genevet, R. Blanchard, Z. Yang, M. M. Qazilbash, D. N. Basov, S. Ramanathan, F. Capasso, *Appl. Phys. Lett.* **2012**, *101*, 221101.
[47] M. J. Dicken, K. Aydin, I. M. Pryce, L. A. Sweatlock, E. M. Boyd, S. Walavalkar, J. Ma, H. A. Atwater, *Opt. Express* **2009**, *17*, 18330.
[48] L. Kang, Q. Zhao, H. Zhao, J. Zhou, *Opt. Express* **2008**, *16*, 8825.
[49] H. Zhao, J. Zhou, L. Kang, Q. Zhao, *Opt. Express* **2009**, *17*, 13373.
[50] S. Chen, Z. Li, W. Liu, H. Cheng, J. Tian, *Adv. Mater.* **2019**, *31*, 1802458.
[51] K. Fan, W. J. Padilla, *Mater. Today* **2015**, *18*, 39.
[52] M. L. Tseng, H. H. Hsiao, C. H. Chu, M. K. Chen, G. Sun, A. Q. Liu, D. P. Tsai, *Adv. Opt. Mater.* **2018**, *6*, 1800554.

[53] X. Zhao, G. Duan, A. Li, C. Chen, X. Zhang, *Microsyst. Nanoeng.* **2019**, *5*, 5.
[54] H. Tao, A. C. Strikwerda, K. Fan, W. J. Padilla, X. Zhang, R. D. Averitt, *Phys. Rev. Lett.* **2009**, *103*, 147401.
[55] W. M. Zhu, A. Q. Liu, X. M. Zhang, D. P. Tsai, T. Bourouina, J. H. Teng, X. H. Zhang, H. C. Guo, H. Tanoto, T. Mei, G. Q. Lo, D. L. Kwong, *Adv. Mater.* **2011**, *23*, 1792.
[56] Z. Chen, M. Rahmani, Y. Gong, T. C. Chong, M. Hong, *Adv. Mater.* **2012**, *24*, 143.
[57] F. Ma, Y. S. Lin, X. Zhang, C. Lee, *Light: Sci. Appl.* **2014**, *3*, e171.
[58] Y.-S. Lin, C. Lee, *Appl. Phys. Lett.* **2014**, *104*, 251914.
[59] T. Kan, A. Isozaki, N. Kanda, N. Nemoto, K. Konishi, H. Takahashi, M. Kuwata-Gonokami, K. Matsumoto, I. Shimoyama, *Nat. Commun.* **2015**, *6*, 8422.
[60] W. Zhu, Q. Song, L. Yan, W. Zhang, P. C. Wu, L. K. Chin, H. Cai, D. P. Tsai, Z. X. Shen, T. W. Deng, S. K. Ting, Y. Gu, G. Q. Lo, D. L. Kwong, Z. C. Yang, R. Huang, A. Q. Liu, N. Zheludev, *Adv. Mater.* **2015**, *27*, 4739.
[61] P. Pitchappa, M. Manjappa, C. P. Ho, R. Singh, N. Singh, C. Lee, *Adv. Opt. Mater.* **2016**, *4*, 541.
[62] X. Zhao, J. Schalch, J. Zhang, H. R. Seren, G. Duan, R. D. Averitt, X. Zhang, *Optica* **2018**, *5*, 303.
[63] M. Manjappa, P. Pitchappa, N. Singh, N. Wang, N. I. Zheludev, C. Lee, R. Singh, *Nat. Commun.* **2018**, *9*, 4056.
[64] E. Cubukcu, S. Zhang, Y.-S. Park, G. Bartal, X. Zhang, *Appl. Phys. Lett.* **2009**, *95*, 043113.
[65] C. Wu, A. B. Khanikaev, R. Adato, N. Arju, A. A. Yanik, H. Altug, G. Shvets, *Nat. Mater.* **2012**, *11*, 69.
[66] R. Adato, H. Altug, *Nat. Commun.* **2013**, *4*, 2154.
[67] O. Limaj, D. Etezadi, N. J. Wittenberg, D. Rodrigo, D. Yoo, S.-H. Oh, H. Altug, *Nano Lett.* **2016**, *16*, 1502.
[68] A. Tittl, A. Leitis, M. Liu, F. Yesilkoy, D. Choi, D. N. Neshev, Y. S. Kivshar, H. Altug, *Science* **2018**, *360*, 1105.
[69] H. Hu, X. Yang, X. Guo, K. Khaliji, S. R. Biswas, F. J. García de Abajo, T. Low, Z. Sun, Q. Dai, *Nat. Commun.* **2019**, *10*, 1131.
[70] T. Maier, H. Brückl, *Opt. Lett.* **2009**, *34*, 3012.
[71] H. Tao, E. A. Kadlec, A. C. Strikwerda, K. Fan, W. J. Padilla, R. D. Averitt, E. A. Shaner, X. Zhang, *Opt. Express* **2011**, *19*, 21620.
[72] W. Ma, Y. Wen, X. Yu, Y. Feng, Y. Zhao, *Appl. Phys. Lett.* **2015**, *106*, 111108.
[73] Y. Hui, J. S. Gomez-Diaz, Z. Qian, A. Alù, M. Rinaldi, *Nat. Commun.* **2016**, *7*, 11249.
[74] C. Belacel, Y. Todorov, S. Barbieri, D. Gacemi, I. Favero, C. Sirtori, *Nat. Commun.* **2017**, *8*, 1578.
[75] Z. Qian, S. Kang, V. Rajaram, C. Cassella, N. E. McGruer, M. Rinaldi, *Nat. Nanotechnol.* **2017**, *12*, 969.
[76] A. Karvounis, B. Gholipour, K. F. MacDonald, N. I. Zheludev, *Adv. Mater.* **2019**, *31*, 1804801.
[77] W. Zhang, W. M. Zhu, J. M. Tsai, G. Q. Lo, D. L. Kwong, E. P. Li, A. Q. Liu, presented at *Proc. IEEE Int. Conf. Micro Electro Mech. Syst.*, Taipei, January **2013**.
[78] W. M. Zhu, A. Q. Liu, T. Bourouina, D. P. Tsai, J. H. Teng, X. H. Zhang, G. Q. Lo, D. L. Kwong, N. I. Zheludev, *Nat. Commun.* **2012**, *3*, 1274.
[79] W. M. Zhu, A. Q. Liu, W. Zhang, J. F. Tao, T. Bourouina, J. H. Teng, X. H. Zhang, Q. Y. Wu, H. Tanoto, H. C. Guo, G. Q. Lo, D. L. Kwong, *Appl. Phys. Lett.* **2011**, *99*, 10.
[80] X. Zhao, K. Fan, J. Zhang, G. R. Keiser, H. R. Seren, R. D. Averitt, X. Zhang, presented at *18th Int. Conf. Solid-State Sensors, Actuators Microsyst.*, Anchorage, AK, June **2015**.
[81] X. Li, T. Yang, W. Zhu, X. Li, *Microsyst. Technol.* **2013**, *19*, 1145.
[82] A. X. Lalas, N. V. Kantartzis, T. D. Tsiboukis, *Microsyst. Technol.* **2015**, *21*, 2097.
[83] X. Zhao, B. Yang, J. Liu, P. Pitchappa, D. Hasan, C. P. Ho, C. Yang, C. Lee, *J. Opt.* **2016**, *18*, 075101.
[84] J. Li, C. M. Shah, W. Withayachumnankul, B. S. Y. Ung, A. Mitchell, S. Sriram, M. Bhaskaran, S. Chang, D. Abbott, *Appl. Phys. Lett.* **2013**, *102*, 121101.
[85] F. Zhang, S. Feng, K. Qiu, Z. Liu, Y. Fan, W. Zhang, Q. Zhao, J. Zhou, *Appl. Phys. Lett.* **2015**, *106*, 091907.
[86] Z. Han, K. Kohno, H. Fujita, K. Hirakawa, H. Toshiyoshi, *IEEE J. Sel. Top. Quantum Electron.* **2015**, *21*, 114.
[87] C. P. Ho, P. Pitchappa, Y.-S. Lin, C.-Y. Huang, P. Kropelnicki, C. Lee, *Appl. Phys. Lett.* **2014**, *104*, 161104.
[88] P. Pitchappa, C. P. Ho, L. Dhakar, Y. Qian, N. Singh, C. Lee, *J. Microelectromech. Syst.* **2015**, *24*, 525.
[89] R. T. Chen, H. Nguyen, M. C. Wu, presented at *12th IEEE Int. Conf. Micro Electro Mech. Syst*, Orlando, FL, USA, January **1999**.
[90] P. Pitchappa, M. Manjappa, H. N. S. Krishnamoorthy, Y. Chang, C. Lee, R. Singh, *Appl. Phys. Lett.* **2017**, *111*, 261101.
[91] Y. S. Lin, C. Lee, *Appl. Phys. Lett.* **2014**, *104*, 251914.
[92] Y.-S. Lin, Y. Qian, F. Ma, Z. Liu, P. Kropelnicki, C. Lee, *Appl. Phys. Lett.* **2013**, *102*, 111908.
[93] Y.-S. Lin, F. Ma, C. Lee, *Opt. Lett.* **2013**, *38*, 3126.
[94] X. Liu, W. J. Padilla, *Adv. Opt. Mater.* **2013**, *1*, 559.
[95] P. Pitchappa, C. P. Ho, L. Dhakar, C. Lee, *Optica* **2015**, *2*, 571.
[96] P. Pitchappa, C. Pei Ho, Y.-S. Lin, P. Kropelnicki, C.-Y. Huang, N. Singh, C. Lee, *Appl. Phys. Lett.* **2014**, *104*, 151104.
[97] L. Cong, P. Pitchappa, C. Lee, R. Singh, *Adv. Mater.* **2017**, *29*, 1700733.
[98] F. Ma, Y.-S. Lin, X. Zhang, C. Lee, *Light: Sci. Appl.* **2014**, *3*, e171.
[99] F. Ma, Y. Qian, Y.-S. Lin, H. Liu, X. Zhang, Z. Liu, J. Ming-Lin Tsai, C. Lee, *Appl. Phys. Lett.* **2013**, *102*, 161912.
[100] Y.-S. Lin, C.-Y. Huang, C. Lee, *IEEE J. Sel. Top. Quantum Electron.* **2015**, *21*, 93.
[101] K. Shih, P. Pitchappa, M. Manjappa, C. P. Ho, R. Singh, B. Yang, N. Singh, C. Lee, *Appl. Phys. Lett.* **2017**, *110*, 161108.
[102] P. Pitchappa, M. Manjappa, C. P. Ho, Y. Qian, R. Singh, N. Singh, C. Lee, *Appl. Phys. Lett.* **2016**, *108*, 111102.
[103] P. Pitchappa, M. Manjappa, C. P. Ho, R. Singh, N. Singh, C. Lee, *Appl. Phys. Lett.* **2016**, *109*, 211103.
[104] L. Cong, P. Pitchappa, Y. Wu, L. Ke, C. Lee, N. Singh, H. Yang, R. Singh, *Adv. Opt. Mater.* **2017**, *5*, 1600716.
[105] C. P. Ho, P. Pitchappa, C. Lee, presented at *Int. Conf. Opt. MEMS Nanophotonics*, Singapore **2016**.
[106] M. Manjappa, P. Pitchappa, N. Wang, C. Lee, R. Singh, *Adv. Opt. Mater.* **2018**, *6*, 1800141.
[107] P. Pitchappa, C. P. Ho, Y. Qian, L. Dhakar, N. Singh, C. Lee, *Sci. Rep.* **2015**, *5*, 11678.
[108] P. Pitchappa, C. P. Ho, L. Cong, R. Singh, N. Singh, C. Lee, *Adv. Opt. Mater.* **2016**, *4*, 391.
[109] R. Adato, A. Artar, S. Erramilli, H. Altug, *Nano Lett.* **2013**, *13*, 2584.
[110] L. Novotny, *Phys. Rev. Lett.* **2007**, *98*, 266802.
[111] V. Giannini, Y. Francescato, H. Amrania, C. C. Phillips, S. A. Maier, *Nano Lett.* **2011**, *11*, 2835.
[112] R. Adato, S. Aksu, H. Altug, *Mater. Today* **2015**, *18*, 436.
[113] L. Verslegers, Z. Yu, P. B. Catrysse, S. Fan, *J. Opt. Soc. Am. B* **2010**, *27*, 1947.
[114] S. Fan, W. Suh, J. D. Joannopoulos, *J. Opt. Soc. Am. A* **2003**, *20*, 569.
[115] C. Chen, D. A. Mohr, H. Choi, D. Yoo, M. Li, S. Oh, *Nano Lett.* **2018**, *18*, 7601.
[116] D. Yoo, D. A. Mohr, F. Vidal-Codina, A. John-Herpin, M. Jo, S. Kim, J. Matson, J. D. Caldwell, H. Jeon, N. Nguyen, L. Martin-Moreno, J. Peraire, H. Altug, S. Oh, *Nano Lett.* **2018**, *18*, 1930.
[117] F. Neubrech, D. Weber, J. Katzmann, C. Huck, A. Toma, E. Di Fabrizio, A. Pucci, T. Härtling, *ACS Nano* **2012**, *6*, 7326.
[118] C. Huck, F. Neubrech, J. Vogt, A. Toma, D. Gerbert, J. Katzmann, T. Härtling, A. Pucci, *ACS Nano* **2014**, *8*, 4908.

[119] X. Chen, C. Wang, Y. Yao, C. Wang, *ACS Nano* **2017**, *11*, 8034.
[120] D. Hasan, C. P. Ho, C. Lee, *ACS Omega* **2016**, *1*, 818.
[121] L. Dong, X. Yang, C. Zhang, B. Cerjan, L. Zhou, M. L. Tseng, Y. Zhang, A. Alabastri, P. Nordlander, N. J. Halas, *Nano Lett.* **2017**, *17*, 5768.
[122] C. P. Ho, P. Pitchappa, B. W. Soon, C. Lee, *Opt. Express* **2015**, *23*, 10598.
[123] C. P. Ho, P. Pitchappa, P. Kropelnicki, J. Wang, H. Cai, Y. Gu, C. Lee, *Opt. Lett.* **2015**, *40*, 2743.
[124] W. C. Tan, L. Wang, X. Feng, L. Chen, L. Huang, X. Huang, K. W. Ang, *Adv. Electron. Mater.* **2019**, *5*, 1.
[125] T. Hu, B. Dong, X. Luo, T.-Y. Liow, J. Song, C. Lee, G.-Q. Lo, *Photonics Res.* **2017**, *5*, 417.
[126] D. Hasan, C. Lee, *Adv. Sci.* **2018**, *5*, 1700581.
[127] Y. Chang, D. Hasan, B. Dong, J. Wei, Y. Ma, G. Zhou, K. W. Ang, C. Lee, *ACS Appl. Mater. Interfaces* **2018**, *10*, 38272.
[128] J. Haase, S. Bagiante, H. Sigg, J. A. van Bokhoven, *Opt. Lett.* **2017**, *42*, 1931.
[129] D. Hasan, P. Pitchappa, C. Pei Ho, C. Lee, *Adv. Opt. Mater.* **2017**, *5*, 1600778.
[130] A. E. Cetin, A. F. Coskun, B. C. Galarreta, M. Huang, D. Herman, A. Ozcan, H. Altug, *Light: Sci. Appl.* **2014**, *3*, e122.
[131] M. Soler, A. Belushkin, A. Cavallini, C. Kebbi-Beghdadi, G. Greub, H. Altug, *Biosens. Bioelectron.* **2017**, *94*, 560.
[132] H. Aouani, M. Rahmani, H. Šípová, V. Torres, K. Hegnerová, M. Beruete, J. Homola, M. Hong, M. Navarro-Cía, S. A. Maier, *J. Phys. Chem. C* **2013**, *117*, 18620.
[133] A. Belushkin, F. Yesilkoy, H. Altug, *ACS Nano* **2018**, *12*, 4453.
[134] J. Garcia-Guirado, R. A. Rica, J. Ortega, J. Medina, V. Sanz, E. Ruiz-Reina, R. Quidant, *ACS Photonics* **2018**, *5*, 3673.
[135] F. Yesilkoy, R. A. Terborg, J. Pello, A. A. Belushkin, Y. Jahani, V. Pruneri, H. Altug, *Light: Sci. Appl.* **2018**, *7*, 17152.
[136] D. Hasan, C. P. Ho, P. Pitchappa, B. Yang, C. Yang, C. Lee, *Sci. Rep.* **2016**, *6*, 22227.
[137] D. Etezadi, J. B. Warner IV, F. S. Ruggeri, G. Dietler, H. A. Lashuel, H. Altug, *Light: Sci. Appl.* **2017**, *6*, e17029.
[138] L. Kühner, M. Hentschel, U. Zschieschang, H. Klauk, J. Vogt, C. Huck, H. Giessen, F. Neubrech, *ACS Sens.* **2017**, *2*, 655.
[139] T. H. H. Le, A. Morita, K. Mawatari, T. Kitamori, T. Tanaka, *ACS Photonics* **2018**, *5*, 3179.
[140] X. Li, M. Soler, C. I. Özdemir, A. Belushkin, F. Yesilköy, H. Altug, *Lab Chip* **2017**, *17*, 2208.
[141] A. F. Coskun, A. E. Cetin, B. C. Galarreta, D. A. Alvarez, H. Altug, A. Ozcan, *Sci. Rep.* **2015**, *4*, 6789.
[142] P. Dey, N. Fabri-Faja, O. Calvo-Lozano, R. A. Terborg, A. Belushkin, F. Yesilkoy, A. Fàbrega, J. C. Ruiz-Rodriguez, R. Ferrer, J. J. González-López, M. C. Estévez, H. Altug, V. Pruneri, L. M. Lechuga, *ACS Sens.* **2019**, *4*, 52.
[143] A. John-Herpin, A. Tittl, H. Altug, *ACS Photonics* **2018**, *5*, 4117.
[144] Y. Zhu, Z. Li, Z. Hao, C. DiMarco, P. Maturavongsadit, Y. Hao, M. Lu, A. Stein, Q. Wang, J. Hone, N. Yu, Q. Lin, *Light: Sci. Appl.* **2018**, *7*, 67.
[145] D. Rodrigo, A. Tittl, N. Ait-Bouziad, A. John-Herpin, O. Limaj, C. Kelly, D. Yoo, N. J. Wittenberg, S.-H. Oh, H. A. Lashuel, H. Altug, *Nat. Commun.* **2018**, *9*, 2160.
[146] P. Su, Z. Han, D. Kita, P. Becla, H. Lin, S. Deckoff-Jones, K. Richardson, L. C. Kimerling, J. Hu, A. Agarwal, *Appl. Phys. Lett.* **2019**, *114*, 051103.
[147] S. Moumen, I. Raible, A. Krauß, J. Wöllenstein, *Sens. Actuators, B.* **2016**, *236*, 1083.
[148] K. J. Kim, X. Chong, P. B. Kreider, G. Ma, P. R. Ohodnicki, J. P. Baltrus, A. X. Wang, C. H. Chang, *J. Mater. Chem. C* **2015**, *3*, 2763.
[149] L. E. Kreno, J. T. Hupp, R. P. Van Duyne, *Anal. Chem.* **2010**, *82*, 8042.
[150] W. Wan, X. Yang, J. Gao, *Opt. Express* **2016**, *24*, 12367.
[151] D. Hasan, C. P. Ho, C. Lee, *Adv. Opt. Mater.* **2016**, *4*, 943.
[152] J. M. Hoffmann, X. Yin, J. Richter, A. Hartung, T. W. W. Maß, T. Taubner, *J. Phys. Chem. C* **2013**, *117*, 11311.
[153] D. Hasan, C. P. Ho, P. Pitchappa, C. Lee, *ACS Photonics* **2015**, *2*, 890.
[154] I. Hwang, J. Yu, J. Lee, J. H. Choi, D. G. Choi, S. Jeon, J. Lee, J. Y. Jung, *ACS Photonics* **2018**, *5*, 3492.
[155] a) J. Paul, R. M. De La Rue, N. P. Johnson, *Proc. SPIE* **2016**, *9883*, 98831C; b) J. Paul, S. G. McMeekin, R. M. De La Rue, N. P. Johnson, *Proc. SPIE* **2017**, *10227*, 102270Z.
[156] A. E. Cetin, M. Turkmen, S. Aksu, D. Etezadi, H. Altug, *Appl. Phys. B* **2015**, *118*, 29.
[157] O. Limaj, D. Etezadi, N. J. Wittenberg, D. Rodrigo, D. Yoo, S. H. Oh, H. Altug, *Nano Lett.* **2016**, *16*, 1502.
[158] B. Špačková, N. S. Lynn, J. Slabý, H. Šípová, J. Homola, *ACS Photonics* **2018**, *5*, 1019.
[159] S. R. Tsai, M. R. Hamblin, *J. Photochem. Photobiol., B* **2017**, *170*, 197.
[160] H. Hoi, S. S. Rezaie, L. Gong, P. Sen, H. Zeng, C. Montemagno, M. Gupta, *Biosens. Bioelectron.* **2018**, *102*, 497.
[161] Z. Li, Y. Zhu, Y. Hao, M. Gao, M. Lu, A. Stein, A.-H. A. Park, J. C. Hone, Q. Lin, N. Yu, *ACS Photonics* **2019**, *6*, 501.
[162] E. Mohammadi, K. L. Tsakmakidis, A. N. Askarpour, P. Dehkhoda, A. Tavakoli, H. Altug, *ACS Photonics* **2018**, *5*, 2669.
[163] D. Rodrigo, O. Limaj, D. Janner, D. Etezadi, F. J. García De Abajo, V. Pruneri, H. Altug, *Science* **2015**, *349*, 165.
[164] F. Yesilkoy, E. R. Arvelo, Y. Jahani, M. Liu, A. Tittl, V. Cevher, Y. Kivshar, H. Altug, *Nat. Photonics* **2019**, *13*, 390.
[165] A. Leitis, A. Tittl, M. Liu, B. H. Lee, M. B. Gu, Y. S. Kivshar, H. Altug, *Sci. Adv.* **2019**, *5*, eaaw2871.
[166] X. Li, M. Soler, C. Szydzik, K. Khoshmanesh, J. Schmidt, G. Coukos, A. Mitchell, H. Altug, *Small* **2018**, *14*, e1800698.
[167] B. Špačková, P. Wrobel, M. Bocková, J. Homola, *Proc. IEEE* **2016**, *104*, 2380.
[168] C. Chen, D. Mohr, H. Choi, D. Yoo, M. Li, S. Oh, *Nano Lett.* **2018**, *26*, 23540.
[169] A. De Marcellis, E. Palange, M. Janneh, C. Rizza, A. Ciattoni, S. Mengali, *Plasmonics* **2017**, *12*, 293.
[170] C. Y. Tsai, J. W. Lin, C. Y. Wu, P. T. Lin, T. W. Lu, P. T. Lee, *Nano Lett.* **2012**, *12*, 1648.
[171] D. Yoo, K. L. Gurunatha, H. Choi, D. A. Mohr, C. T. Ertsgaard, R. Gordon, S. Oh, *Nano Lett.* **2018**, *18*, 3637.
[172] D. Yoo, D. A. Mohr, F. Vidal-Codina, A. John-Herpin, M. Jo, S. Kim, J. Matson, J. D. Caldwell, H. Jeon, N. Nguyen, L. Martin-Moreno, J. Peraire, H. Altug, S. Oh, *Nano Lett.* **2018**, *18*, 1930.
[173] T. H. H. Le, T. Tanaka, *ACS Nano* **2017**, *11*, 9780.
[174] K. Shih, Z. Ren, C. Wang, C. Lee, *J. Phys. D: Appl. Phys.* **2019**, https://doi.org/10.1088/1361-6463/ab2ea1.
[175] M. Navarro-Cia, S. A. Maier, *ACS Nano* **2012**, *6*, 3537.
[176] S. Gottheim, H. Zhang, A. O. Govorov, N. J. Halas, *ACS Nano* **2015**, *9*, 3284.
[177] D. Rodrigo, A. Tittl, A. John-Herpin, O. Limaj, H. Altug, *ACS Photonics* **2018**, *5*, 4903.
[178] S. Oh, H. Altug, *Nat. Commun.* **2018**, *9*, 5263.
[179] E. Aslan, E. Aslan, R. Wang, M. K. Hong, S. Erramilli, M. Turkmen, O. G. Saracoglu, L. Dal Negro, *ACS Photonics* **2016**, *3*, 2102.
[180] A. A. Abduljabar, D. J. Rowe, A. Porch, D. A. Barrow, *IEEE Trans. Microwave Theory Tech.* **2014**, *62*, 679.
[181] P. Velez, L. Su, K. Grenier, J. Mata-Contreras, D. Dubuc, F. Martin, *IEEE Sens. J.* **2017**, *17*, 6589.
[182] A. Salim, S. Lim, *Sensors* **2016**, *16*, 1802.
[183] R. A. Awang, F. J. Tovar-Lopez, T. Baum, S. Sriram, W. S. T. Rowe, *J. Appl. Phys.* **2017**, *121*, 094506.
[184] K. Ling, M. Yoo, W. Su, K. Kim, B. Cook, M. M. Tentzeris, S. Lim, *Opt. Express* **2015**, *23*, 110.
[185] H. Kim, D. Lee, S. Lim, *Sensors* **2016**, *16*, 1246.

[186] M. Yoo, H. K. Kim, S. Lim, *Sens. Actuators, B.* **2016**, *222*, 173.
[187] Y. Seo, M. U. Memon, S. Lim, *IEEE Trans. Antennas Propag.* **2016**, *64*, 3218.
[188] K. Jaruwongrungsee, U. Waiwijit, W. Withayachumnankul, presented at *Proc. 2015 IEEE 15th Int. Conf. Nanotechnol (IEEE-NANO)*, Rome, Italy **2015**.
[189] R. Sista, Z. Hua, P. Thwar, A. Sudarsan, V. Srinivasan, A. Eckhardt, M. Pollack, V. Pamula, *Lab Chip* **2008**, *8*, 2091.
[190] J. El-Ali, P. K. Sorger, K. F. Jensen, *Nature* **2006**, *442*, 403.
[191] M. Islam, S. J. M. Rao, G. Kumar, B. P. Pal, D. Roy Chowdhury, *Sci. Rep.* **2017**, *7*, 7355.
[192] F. Miyamaru, K. Hattori, K. Shiraga, S. Kawashima, S. Suga, T. Nishida, M. W. Takeda, Y. Ogawa, *J. Infrared, Millimeter, Terahertz Waves* **2014**, *35*, 198.
[193] H. R. Park, K. J. Ahn, S. Han, Y. M. Bahk, N. Park, D. S. Kim, *Nano Lett.* **2013**, *13*, 1782.
[194] D.-K. Lee, J. Kang, J.-S. Lee, H.-S. Kim, C. Kim, J. Hun Kim, T. Lee, J. Son, Q. Park, M. Seo, *Sci. Rep.* **2015**, *5*, 15459.
[195] S. J. Park, J. T. Hong, S. J. Choi, H. S. Kim, W. K. Park, S. T. Han, J. Y. Park, S. Lee, D. S. Kim, Y. H. Ahn, *Sci. Rep.* **2015**, *4*, 4988.
[196] A. Berrier, M. C. Schaafsma, G. Nonglaton, J. Bergquist, J. G. Rivas, *Biomed. Opt. Express* **2012**, *3*, 2937.
[197] D.-K. Lee, J. Kang, J. Kwon, J.-S. Lee, S. Lee, D. H. Woo, J. H. Kim, C. Song, Q. Park, M. Seo, *Sci. Rep.* **2017**, *7*, 8146.
[198] A. P. Tenggara, S. J. Park, H. T. Yudistira, Y. H. Ahn, D. Byun, *J. Micromech. Microeng.* **2017**, *27*, 035009.
[199] S. J. Park, B. H. Son, S. J. Choi, H. S. Kim, Y. H. Ahn, *Opt. Express* **2014**, *22*, 30467.
[200] F. Hu, E. Guo, X. Xu, P. Li, X. Xu, S. Yin, Y. Wang, T. Chen, X. Yin, W. Zhang, *Opt. Commun.* **2017**, *388*, 62.
[201] S. J. Park, S. A. N. Yoon, Y. H. Ahn, *RSC Adv.* **2016**, *6*, 69381.
[202] Z. Geng, X. Zhang, Z. Fan, X. Lv, H. Chen, *Sci. Rep.* **2017**, *7*, 16378.
[203] K. Shih, P. Pitchappa, M. Manjappa, C. P. Ho, R. Singh, C. Lee, *J. Appl. Phys.* **2017**, *121*, 023102.
[204] K. Serita, E. Matsuda, K. Okada, H. Murakami, I. Kawayama, M. Tonouchi, *APL Photonics* **2018**, *3*, 051603.
[205] K. Shih, P. Pitchappa, L. Jin, C.-H. Chen, R. Singh, C. Lee, *Appl. Phys. Lett.* **2018**, *113*, 071105.
[206] F. Niklaus, C. Vieider, H. Jakobsen, in *MEMS/MOEMS Technologies and Applications III* (Vol. *6836*), SPIE, Bellingham, WA **2007**, p. 68360D.
[207] H. Zhou, P. Kropelnicki, J. M. Tsai, C. Lee, *J. Micromech. Microeng.* **2013**, *23*, 065026.
[208] H. Zhou, P. Kropelnicki, C. Lee, *J. Microelectromech. Syst.* **2015**, *24*, 144.
[209] C. M. Watts, X. Liu, W. J. Padilla, *Adv. Mater.* **2012**, *24*, OP98.
[210] S. Ogawa, K. Okada, N. Fukushima, M. Kimata, *Appl. Phys. Lett.* **2012**, *100*, 021111.
[211] S. Ogawa, K. Masuda, Y. Takagawa, M. Kimata, *Opt. Eng.* **2014**, *53*, 107110.
[212] S. Ogawa, Y. Takagawa, M. Kimata, *Sens. Actuators, A.* **2018**, *269*, 563.
[213] J. Y. Ou, E. Plum, J. Zhang, N. I. Zheludev, *Adv. Mater.* **2016**, *28*, 729.
[214] M. Lapine, I. V. Shadrivov, Y. S. Kivshar, *Rev. Mod. Phys.* **2014**, *86*, 1093.
[215] J. Valentine, S. Zhang, T. Zentgraf, E. Ulin-Avila, D. A. Genov, G. Bartal, X. Zhang, *Nature* **2008**, *455*, 376.
[216] N. Liu, H. Guo, L. Fu, S. Kaiser, H. Schweizer, H. Giessen, *Nat. Mater.* **2008**, *7*, 31.
[217] F. Miyamaru, S. Kuboda, K. Taima, K. Takano, M. Hangyo, M. W. Takeda, *Appl. Phys. Lett.* **2010**, *96*, 081105.
[218] C. M. Soukoulis, M. Wegener, *Nat. Photonics* **2011**, *5*, 523.
[219] H. O. Moser, C. Rockstuhl, *Laser Photonics Rev.* **2012**, *6*, 219.
[220] J. Rogers, Y. Huang, O. G. Schmidt, D. H. Gracias, *MRS Bull.* **2016**, *41*, 123.
[221] Y. Zhang, F. Zhang, Z. Yan, Q. Ma, X. Li, Y. Huang, J. A. Rogers, *Nat. Rev. Mater.* **2017**, *2*, 17019.
[222] H. Fu, K. Nan, W. Bai, W. Huang, K. Bai, L. Lu, C. Zhou, Y. Liu, F. Liu, J. Wang, M. Han, Z. Yan, H. Luan, Y. Zhang, Y. Zhang, J. Zhao, X. Cheng, M. Li, J. W. Lee, Y. Liu, D. Fang, X. Li, Y. Huang, Y. Zhang, J. A. Rogers, *Nat. Mater.* **2018**, *17*, 268.
[223] Q. Zhang, X. Xu, D. Lin, W. Chen, G. Xiong, Y. Yu, T. S. Fisher, H. Li, *Adv. Mater.* **2016**, *28*, 2229.
[224] D. B. Burckel, J. R. Wendt, G. A. Ten Eyck, J. C. Ginn, A. R. Ellis, I. Brener, M. B. Sinclair, *Adv. Mater.* **2010**, *22*, 5053.
[225] D. B. Burckel, J. R. Wendt, G. A. Ten Eyck, A. R. Ellis, I. Brener, M. B. Sinclair, *Adv. Mater.* **2010**, *22*, 3171.
[226] J. H. Cho, M. D. Keung, N. Verellen, L. Lagae, V. V. Moshchalkov, P. Van Dorpe, D. H. Gracias, *Small* **2011**, *7*, 1943.
[227] S. Vignolini, N. A. Yufa, P. S. Cunha, S. Guldin, I. Rushkin, M. Stefik, K. Hur, U. Wiesner, J. J. Baumberg, U. Steiner, *Adv. Mater.* **2012**, *24*, OP23.
[228] D. Chanda, K. Shigeta, S. Gupta, T. Cain, A. Carlson, A. Mihi, A. J. Baca, G. R. Bogart, P. Braun, J. A. Rogers, *Nat. Nanotechnol.* **2011**, *6*, 402.
[229] Z. Liu, H. Du, J. Li, L. Lu, Z.-Y. Li, N. X. Fang, *Sci. Adv.* **2018**, *4*, eaat4436.
[230] A. Kuzyk, R. Schreiber, H. Zhang, A. O. Govorov, T. Liedl, N. Liu, *Nat. Mater.* **2014**, *13*, 862.
[231] K. Fuchi, A. R. Diaz, E. J. Rothwell, R. O. Ouedraogo, J. Tang, *J. Appl. Phys.* **2012**, *111*, 084905.
[232] Z. Wang, L. Jing, K. Yao, Y. Yang, B. Zheng, C. M. Soukoulis, H. Chen, Y. Liu, *Adv. Mater.* **2017**, *29*, 1700412.